Review

International Journal of Modern Physics B
Vol. 19, No. 31 (2005) 4525–4565

World Scientific
www.worldscientific.com

MULTISCALE MODELING OF SOLIDIFICATION: PHASE-FIELD METHODS TO ADAPTIVE MESH REFINEMENT

NIKOLAS PROVATAS and MICHAEL GREENWOOD

Department of Materials Science and Engineering,
and Brockhouse Institute for Materials Research, McMaster University,
1280 Main Street West, Hamilton, Ontario, L8S 4L7, Canada

BADRINARAYAN ATHREYA and NIGEL GOLDENFELD

Department of Physics, University of Illinois at Urbana-Champaign,
Urbana, IL 61801, USA

JONATHAN DANTZIG

Department of Mechanical and Industrial Engineering,
University of Illinois at Urbana-Champaign, Urbana, IL 61801, USA

Received 25 August 2005

We review the use of phase field methods in solidification modeling, describing their fundamental connection to the physics of phase transformations. The inherent challenges associated with simulating phase field models across multiple length and time scales are discussed, as well as how these challenges have been addressed in recent years. Specifically, we discuss new asymptotic analysis methods that enable phase field equations to emulate the sharp interface limit even in the case of quite diffuse phase-field interfaces, an aspect that greatly reduces computation times. We then review recent dynamic adaptive mesh refinement algorithms that have enabled a dramatic increase in the scale of microstructures that can be simulated using phase-field models, at significantly reduced simulation times. Combined with new methods of asymptotic analysis, the adaptive mesh approach provides a truly multi-scale capability for simulating solidification microstructures from nanometers up to centimeters. Finally, we present recent results on 2D and 3D dendritic growth and dendritic spacing selection, which have been made using phase-field models solved with adaptive mesh refinement.

Keywords: Solidification; phase-field models; adaptive mesh refinement; multiscale modeling; microstructure selection.

PACS Number(s): 81.30.Fb, 68.70.+w

1. Introduction

The physics of solidification underlies many important processes of scientific and industrial importance. Solidification microstructures establish the fundamental length scales that influence the material properties of cast alloys.[1] Our understanding of

microstructure formation in traditional thick-slab casting technologies has been well developed over the past few decades.[2] However, a unified prediction of length scale selection and microstructural growth kinetics as a function of processing and material parameters is still lacking. This is particularly true in technologies involving rapid solidification, where alloys inherit many of the as-cast microstructure properties.

Experimental solidification research in metals often relies on empirical parameter searches required to link microstructural characteristics with processing regimes, and is often limited in its ability to observe real-time development of microstructure and the associated segregation patterns. To this end, recent work in computational modeling has proved to be an "emerging technology" that complements experimental research. Numerical simulations can guide experiments, as well as define relevant parametric ranges to be studied. Designing experiments based on predictions from numerical simulations can thus help to better understand alloy microstructure formation in a systematic, efficient and cost effective manner.

The greatest challenge in solidification modeling involves the multi-scale nature of solidification microstructures. Liquid-solid interfaces are on the order of a few nanometers thick, whereas relevant microstructural features are on the scale of tens to hundreds of microns. Moreover, the time scales involved in solidification span from picoseconds for atomic attachment kinetics, to seconds for diffusion of heat and solute. Capturing the physics of solidification over such multiple length scales, while still capturing long enough times to make contact with experiments requires innovations in both mathematical models and numerical simulation techniques.

This article discusses new developments in multi-scale modeling of solidification. We review recent innovations in dynamic adaptive mesh refinement (DAMR) techniques, and discuss new developments in phase-field asymptotics that enable efficient simulation of solidification microstructures. Section 2 begins by reviewing sharp-interface models of solidification. Section 3 reviews the phase-field method and its application to modeling solidification of pure materials and binary alloys. We also discuss new advances in phase-field asymptotics that allow us to recover the physics of sharp-interface models of solidification in the limit of diffuse phase-field interfaces. This feature permits the modeling of experimentally relevant time scales. In Sec. 4 we review a novel dynamic adaptive-mesh refinement technique specifically designed for phase-field models of solidification. DAMR enables the resolution of microstructures from the scale of the interface width up to the scale of millimeters. Coupled with phase-field asymptotics and modern parallel computing, DAMR provides the closest approximation to date of a truly multi-scale methodology for simulating solidification. Section 5 reviews recent work in microstructure selection in two spatial dimensions. This includes morphological scaling in dendritic growth and dendritic spacing selection in directional solidification. Section 6 reviews recent work on coupling dendritic growth to fluid flow using adaptive mesh refinement in three dimensions.

2. Kinetics of Solidification

Traditional approaches to modeling solidification have often use so-called *sharp-interface* models to describe the physics of dendritic growth. For solidification of pure materials the sharp-interface model describes diffusion of heat in the solid and liquid phases, heat flux conservation across a mathematically sharp solid-liquid interface and the depression of local interfacial melting temperature due to curvature and interface kinetics. In alloy solidification, at low to moderate undercooling, solute transport is the rate-limiting step because the ratio of solutal to thermal diffusivity is small. For this reason, one often neglects heat transport when considering alloys. In this limit, the mathematical description of solidification of a pure material is mathematically equivalent to the solidification of a dilute binary alloy.[3]

Isothermal solidification of an alloy is described by solute diffusion in each phase, expressed as

$$\frac{\partial C(\vec{x},t)}{\partial t} = \nabla \cdot (D \nabla C(\vec{x},t)) \tag{1}$$

where $C(\vec{x},t)$ is the solute concentration field in either the solid or liquid phase and D is the diffusivity. Conservation of mass at the solid-liquid interface is described by

$$D_S \nabla C|_S \cdot \vec{n} - D_L \nabla C|_L \cdot \vec{n} = (C_L - C_S) V_n \tag{2}$$

where the subscripts S and L indicate the solid and liquid phases at the interface, respectively, $\vec{n}$ is the local interface normal vector and V_n is the local normal interface speed. For a flat interface, the concentrations at the interface are given by the equilibrium phase-diagram. Figure 1 illustrates a generic isomorphous binary alloy phase diagram. For dilute alloys, a simplification is often made by assuming that the liquidus and solidus are straight lines with slopes m_L and m_S, respectively and where the partition coefficient $C_S/C_L = k$ is constant. For larger concentrations k is not in general a constant. The work presented in Secs. 5 and 6 is restricted to the dilute limit.

When the interface is curved and moving, the local concentration on the liquid side of the interface is depressed from its equilibrium value C_{eq}^L according to

$$\frac{C_L - C_{\text{eq}}^L}{\Delta C_o} = -d_o^c \kappa - \beta V_n \tag{3}$$

with $d_o^c = d_o/\Delta T$, where $d_o = \gamma T_M/L$ is the capillary length, γ is the surface tension energy, T_M is the melting temperature and L is the latent heat of fusion (of component A of the A-B alloy). Also, $\Delta C_o = C_{\text{eq}}^L - C_{\text{eq}}^S$. The parameter β is the interface kinetics coefficient and κ is twice the mean curvature of the interface. For dilute alloys the freezing range of the alloy of initial concentration C_o^l is given by $\Delta T = |m_L|(1-k)C_o^l$. In pure materials $d_o \approx 10^{-8}$ m, while the chemical capillary length can be significantly larger for dilute alloys. In general d_o^c and β are anisotropic, reflecting the variation of surface tension energy and attachment kinetics with crystalline orientation. We denote this dependence on interface orientation

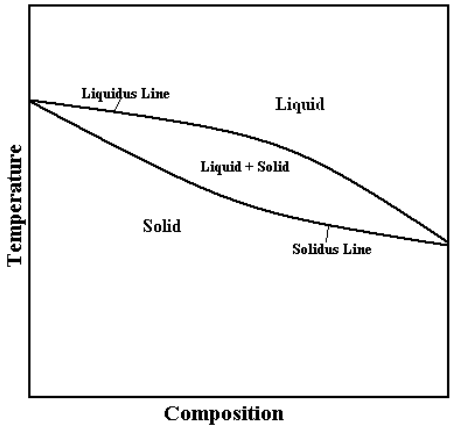

Fig. 1. Isomorphouse binary alloy phase diagram.

as $d_o^c(\vec{n})$ and $\beta(\vec{n})$, where $\vec{n}$ denotes the local interface normal. Typical forms for the capillary length and kinetic coefficient that exhibit m-fold and p-fold anisotropy can be expressed as $d_o^c(\vec{n}) = d_o^c[1 - \epsilon_m \cos(m\theta)]$ and $\beta(\vec{n}) = \beta_o[1 + \epsilon_p \cos(p\theta)]$, where θ denotes the angle the unit normal to the interface, $\vec{n}$, makes with a reference axis. All cases presented here have $m = p = 4$, corresponding to cubic crystalline symmetry.

For very rapid solidification rates (i.e. $V_n > 1$ m/s) the interface width and solute diffusion length are comparable and the behavior at the solid-liquid interface is no longer well represented by Eq. (3). In the dilute alloy limit, the chemical potential difference across the interface is given by[4]

$$\mu_L - \mu_S = -\frac{(C_L - C_S)W_o}{M_L C_L(1 - C_L)} V_n \tag{4}$$

where W_o denotes the interface width, V_n is the interface velocity and M_L is the solute mobility. Models of rapid solidification[4–9] assume that the driving force for solidification is reduced by the amount of energy dissipated within the diffuse interface during solidification.[7] These considerations lead to an effective relation between the interface temperature and concentration given by[9]

$$T = T_M + m_L \frac{(1-k) + [k + \alpha(1-k)]\ln(k/k_E)}{1 - k_E} C_L - \beta V_n \tag{5}$$

where k is a non-equilibrium partition coefficient given by

$$k(V_n) = \frac{k_E + V_n/V_D}{1 + V_n/V_D} \tag{6}$$

where k_E represents the equilibrium partition coefficient and $V_D \approx D_I/W_o$ and D_I is the interface diffusion coefficient. The parameter α is referred to as the solute drag coefficient. Solute drag models for rapid solidification are summarized in Ref. 10 and references therein, and will not be considered further in this work.

Numerical simulation of solidification using sharp interface models poses significant computational problems. Boundary conditions must be applied at a singular interface, requiring the interface to be explicitly tracked. For polycrystalline growth, which involves complicated interface topologies, the problem of interface tracking becomes non-trivial to implement, particularly in 3D. Furthermore, for many non-equilibrium phenomena, the sharp interface limit is not known *a priori*[11] and the simplest fundamental description of a system is obtained by minimization of its free energy, written in terms of continuous fields.

3. Phase-Field Models of Solidification

3.1. *Phenomenology: Pure materials*

We begin here with a brief review of the phase-field method by examining the well-documented case of the solidification of a pure material.[12–21] The phase field method begins with a phenomenological *free energy* (F) of the solid-liquid system expressed in terms of the temperature and the order parameter field $\phi(x)$ that takes fixed values in either phase (e.g. $\phi = -1$ in the liquid and $\phi = 1$ in the solid) and continuously interpolates between these values across a thin interface whose width is denoted by W_ϕ. The interface is defined as the level set of points satisfying $\phi(\vec{x}, t) = C_i$, where $-1 < C_i < 1$.[17] A form of F for a pure material is given by

$$F[\phi, U] = \int (|W_\phi(\vec{n})\nabla\phi|^2 + h(\phi) - \lambda U P(\phi))dV \tag{7}$$

where $U = (T - T_M)/(L/c_p)$ is the dimensionless temperature field, T_M is the melting temperature, L is the latent heat of fusion and c_p is the specific heat at

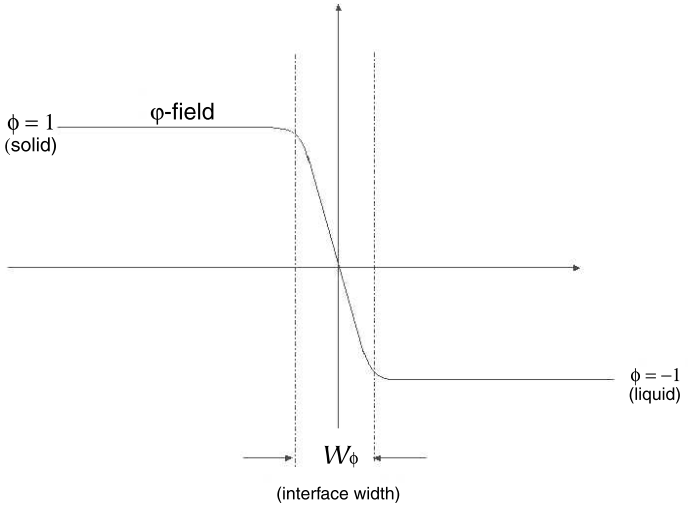

Fig. 2. Schematic of an interface of the phase field in 1D. The solid phase has a value of $\phi = 1$, a smooth transition through the interface and a value of $\phi = -1$ in the liquid.

constant pressure. The constant λ is proportional to the inverse of the nucleation energy. In cases where we are not concerned with modeling nucleation kinetics but, rather, the kinetics of dendritic growth, λ can be treated as a free parameter. The expression $|W_\phi(\vec{n})\nabla\phi|^2$ controls the surface tension energy, made anisotropic through the function $W_\phi(\vec{n}) = W_o A(\vec{n})$,[18,22] where $\vec{n}$ is the local normal to the interface and W_o denotes the isotropic liquid-solid interface width. A typical form often used for $A(\vec{n})$ is given by[18,20,22–27]

$$A(\vec{n}) = [1 - 3\epsilon_4]\left[1 + \frac{4\epsilon_4}{(1 - 3\epsilon_4)}((n_x)^4 + (n_y)^4 + (n_z)^4)\right] \tag{8}$$

where ϵ_4 controls the 4-fold anisotropy strength. The function $h(\phi) = -\phi^2/2 + \phi^4/4$ is the so-called "double-well" potential that separates the energy between the solid and liquid phases. The function $P(\phi)$ is an algebraic function that assumes the limits $P(\pm 1) = \pm 1$ and $P'(\pm 1) = 0$. In the sharp interface limit of phase-field models, the specific form of $P(\phi)$ in the interface is not important, as all that enters the analysis are its limits at $\phi = \pm 1$.[17,18,26–28] A convenient choice, which maintains the bulk phases at $\phi = \pm 1$ is $P(\phi) = \phi - \phi^3/3 + \phi^5/5$. Its form is shown in Fig. 3, which illustrates the relative changes in the free energy between the bulk solid($\phi = +1$) and liquid($\phi = -1$) as the temperature changes.

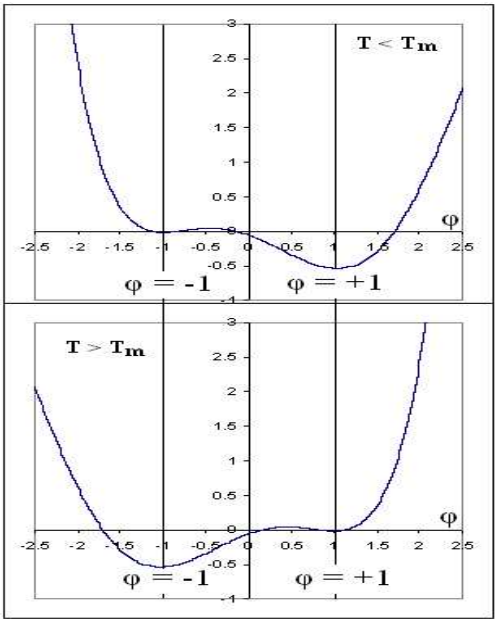

Fig. 3. Free energy density for a pure materials. Top: $T < T_M$ the well shifts toward the solid. Bottom: $T > T_M$ the well shifts to the liquid.

The evolution equation for ϕ is described by dissipative minimization of the free energy, expressed as

$$\begin{aligned}\tau(\vec{n})\frac{\partial\phi}{\partial t} &= -\frac{\delta F}{\delta\phi} + \xi(\vec{x},t) \\ &= W_\phi^2(\vec{n})\nabla^2\phi + \phi - \phi^3 - \lambda U(1-\phi^2)^2 \\ &\quad + W_o\frac{1}{2}\boldsymbol{\nabla}\cdot\left[|\nabla\phi|^2\frac{\partial A^2(\vec{n})}{\partial(\boldsymbol{\nabla}\phi)}\right] + \xi(\vec{x},t) \end{aligned} \tag{9}$$

where $\tau(\vec{n}) = \tau_o B(\vec{n})$ represents the anisotropic interface kinetic attachment time scale, with τ_o a constant. The stochastic variable $\xi(\vec{x},t)$ represents noise due to thermal fluctuations, chosen from a random distribution whose moments satisfy the fluctuation-dissipation theorem,[29] $\langle\xi(\vec{x},t)\xi(\vec{x}',t')\rangle = 2T/\tau_o\delta(\vec{x}-\vec{x}')\delta(t-t')$, where α is the thermal diffusion coefficient, k_B is Boltzmann's constant and $\delta(x)$ is the Dirac delta function. The fluctuation-dissipation theorem ensures interface fluctuates consistently with statistical thermodynamics. When the function $B(\vec{n}) = A(\vec{n})$, it is possible to simulate the limit of $\beta = 0$ of the sharp interface model, even for large ratios[18] of W_o/d_o (discussed further below). For a constant temperature, Eq. (9) is often referred to as *Model A*[21] and describes the evolution of a single, non-conserved order parameter field.

The evolution of ϕ is coupled to the dynamics of the temperature field via a modified form of the heat diffusion equation

$$\frac{\partial U}{\partial t} = \nabla\cdot(\alpha\nabla U) + \frac{1}{2}\frac{\partial\phi}{\partial t} + \eta(\vec{x}.t) \tag{10}$$

where α is the thermal diffusivity. The second term on the right hand side of Eq. (10) represents the latent heat released during solidification, as illustrated in Fig. 4. This form "smears" the latent heat across the diffuse region of the interface, and reduces to a delta function source in the sharp-interface limit $W_o \to 0$. The stochastic noise

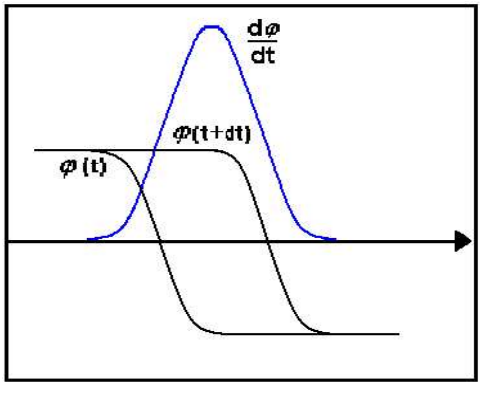

Fig. 4. Schematic of an advancing interface. The interface advances essentially as a propagating front. The quantity $\partial\phi/\partial t$ represents a normalized quantity of heat released at the interface.

term satisfies $\langle \eta(\vec{x},t)\eta(\vec{x}',t')\rangle = 2\alpha k_B T/c_p \nabla^2 \delta(\vec{x}-\vec{x}')\delta(t-t')$.[29] Equations (9) and (10) can be conveniently studied in dimensionless form by rescaling space as $x \to x/W_o$ and time as $t \to t/\tau_o$. In that case we can treat $\tau_o = W_o = 1$ in Eq. (9), while $D \to D\tau_o/W_o^2$ in Eq. (10).

The parameters of the phase-field model can be selected to recover the dynamics of the sharp interface limit. This can formally be achieved by letting $W_o \to 0$ and $\lambda \to 0$, such that $W_o/\lambda \sim d_o$ and $\tau_o/\lambda W_o \sim \beta$.[27,20] To simulate the important case of $\beta = 0$, use of these relationships would require that the simulation time scale τ_o become prohibitively small, as would the minimum mesh spacing. This asymptotic limit is of little practical value when there is a significant disparity between the capillary length d_o and the diffusion length D/V. Since the interface width is of order 10^{-9} m, this precludes simulation of large-scale dendritic structures over a significant amount of time. An improvement in the asymptotic mapping of the phase-field model to the sharp interface model, when the thermal conductivities are equal in the two phases, was developed in Ref. 18. That work showed that the sharp-interface limit can be faithfully reproduced if the interface width (W_o), the kinetics time (τ_o) and the coupling parameter (λ) are inter-related according to

$$d_o = a_1 \frac{W_o}{\lambda} \tag{11}$$

and

$$\beta = \frac{a_1 \tau_o}{W_o \lambda}\left(1 - a_2 \lambda \frac{W_o^2}{D_L \tau_o}\right) \tag{12}$$

where a_1 and a_2 are constants that depend of integrals of the steady-state phase-field function ϕ_o. For our choice of the phase-field model described above, $a_1 = 0.8839$ and $a_2 = 0.6267$. The remarkable feature of Eq. (12) is that it allows us to simulate the $\beta = 0$ limit even for large values of the ratio W_o/d_o merely by choosing an appropriate interface kinetics time scale τ_o. Combining such asymptotic matching results with adaptive mesh refinement algorithms (discussed in Sec. 4)[30,31] enabled, for the first time, simulations of dendritic structures at experimentally relevant undercooling. Figure 5 shows a thermal dendrite simulated at dimensionless undercooling $\Delta = 0.55$ for a ratio $W_o/d_o \approx 4$ in a system size that would require over 6400×6400 nodes on a uniform grid. Other algorithms, involving the use of random walkers to solve the diffusion equation in the liquid phase, have also been developed to simulate isolated dendritic growth.[32,33] These algorithms are fairly easy to implement but limited in their application to simple interface topologies.

3.2. *Solidification of binary alloys*

The phase field concept for pure materials has also been extended to simulate transformations in binary alloys (components A and B).[4,14,15,17,23,25,26,34–38] The order parameter field ϕ is now coupled to a concentration field C and the temperature

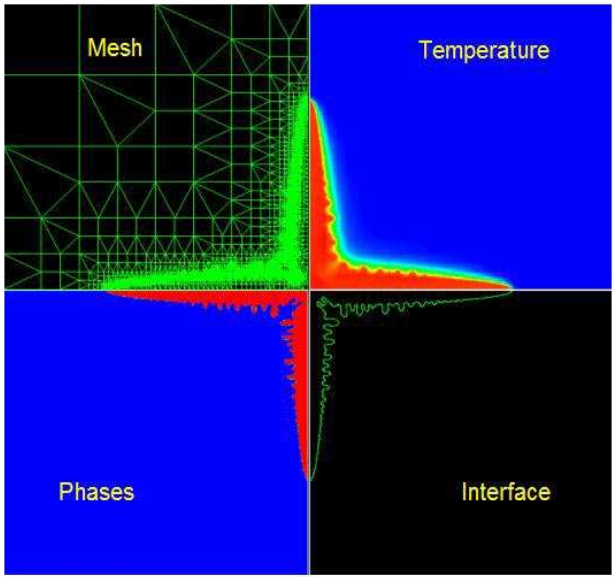

Fig. 5. Snapshot in time of a thermal dendrite grown at $\Delta = c_p(T_m - T)/L = 0.55$ using adaptive mesh refinement (see Sec. 4). The four views represent: (top right) temperature, with lighter(darker) shades of gray representing higher(lower) temperatures; (bottom left) phase-field, with the darker field representing liquid and the lighter field solid; (bottom right) solid-liquid interface; (top left) dynamic FEM mesh.

field T (in this case, $\phi = 0$ is liquid and $\phi = 1$ is solid). A free energy functional for a general binary alloy is written as

$$\bar{F} = \int |\epsilon_\phi(\vec{n})\nabla\phi|^2 + |\epsilon_c(\vec{n})\nabla C|^2 + \bar{f}_{AB}(\phi, C, T)]dV \tag{13}$$

where ϵ_ϕ and ϵ_c $(\sqrt{J/m})$ set an energy scale for the order parameter and compositional[39,40] interfaces. The corresponding width of these interfaces is given, respectively, by $W_c = \epsilon_c/\sqrt{\Lambda}$ and $W_\phi = \epsilon_\phi/\sqrt{\Lambda}$, where Λ (J/m^3) denotes the energy barrier between solid and liquid phases, and is proportional to the solid-liquid surface energy (assumed here to be the same for both A and B materials). Both ϵ_c and ϵ_ϕ are made anisotropic by making them functions of the interface normal $\vec{n}$. The function $\bar{f}_{AB}$ denotes the bulk free energy density of the A-B mixture. Its is designed to reproduce the thermodynamic phase diagram of the alloy.

The simplest form of $\bar{f}_{AB}$ is written as[4,23,25]

$$\bar{f}_{AB} = (1 - C)\bar{f}_A(\phi, T) + C\bar{f}_B(\phi, T) + \frac{RT}{v_m}\left[C \ln C + (1 - C)\ln(1 - C)\right]$$
$$+ \frac{RT}{v_m} C(1 - C)[M_S H(\phi) + M_L(1 - H(\phi))] \tag{14}$$

where v_m denotes the molar volume of solid A and B phases and $H(\phi)$ is an interpolation function with limits $H(1) = 1$ (solid) and $H(0) = 0$ (liquid) and M_S,

M_L are constants. The functions $\bar{f}_{A,B}$ represent the free energy densities of pure A and B, respectively. An explicit form for $\bar{f}_{A,B}$ is given by[4,23]

$$\bar{f}_{A,B} = \Lambda g(\phi) - \frac{L_{A,B}(T - T_{A,B})}{T_{A,B}}(1 - P(\phi)) \tag{15}$$

where $L_{A,B}$ and $T_{A,B}$ are the latent heats of fusion and melting temperatures of A and B, respectively. The function $g(\phi) = \phi^2(1-\phi)^2$ provides a double-well potential between solid and liquid phases, while $P(\phi) = \phi^2(3 - 2\phi)$ is a convenient function that interpolates between the solid and liquid entropy states (we define the solid phase as the reference state of entropy density). The first two terms on the right hand side of Eq. (14) describes the bulk energy of independent alloy components in solid or liquid, weighted by their respective concentrations. The third term describes the energy of ideal mixing between A-B atoms. Finally, the second line describes the interaction energy between the two components, modulated in each phase via the function $H(\phi)$.

Through the interdiffusion (chemical) potential $\mu = \partial \bar{f}_{AB}/\partial C$, the phase-diagram of the A-B alloy can be constructed via the Maxwell equal area construction (the common tangent rule) by solving for the values of C_S, C_L and $\mu_{\rm eq}$ that satisfy the equation

$$\int_{C_S}^{C_L} \left(\frac{\partial \bar{f}_{AB}(\phi, C, T)}{\partial C} - \mu_{\rm eq}(T) \right) dC = 0\,. \tag{16}$$

For example, it is a straight forward exercise to show that by setting $M_L = 0$ and $M_s = (44600 - 9.19T) - (5600 - 1.73T)(2C - 1)$ in Eq. (14), Eq. (16) will yield a eutectic phase-diagram very close to that of Ag-Cu. Setting $M_S = M_L = 0$, Eq. (16) will yield an isomorphous phase diagram.

An important limit of Eq. (14) is in the dilute limit, $C \ll 1$, where the solidus and liquidus can be approximated by straight lines, and where $C_S/C_L = k_E$ for all temperatures, in equilibrium. The free energy for this case is obtained by expanding Eq. (14) to lowest order in C, giving

$$\bar{f}_{AB} = \Lambda g(\phi) + f_A(T_M) - \Delta T S(\phi) + G(\phi)C + \frac{RT_M}{v_m}(C \ln C - C) \tag{17}$$

where $S(\phi) = L_A/T_A(1 - P(\phi))$ is the entropy density of the alloy, and $G(\phi) = -(T - T_B)L_B/T_B(1 - P(\phi))$ is the energy density of adding B to A. We note that other forms of $S(\phi)$ and $G(\phi)$ can also be used for the entropy and energy, yielding equivalent results.[26]

The phase-field equation for alloys is similar to that for pure materials,

$$\tau(\vec{n})\frac{\partial \phi}{\partial t} = -\frac{\delta F}{\delta \phi} + \xi(\vec{x}, t) \tag{18}$$

where we have defined $F \equiv \bar{F}/\Lambda$. Solute transport in the alloy is described by conservation of mass,

$$\frac{\partial C}{\partial t} = -\nabla \cdot \vec{J}. \tag{19}$$

The solute flux $\vec{J}$ is given by

$$\vec{J} = M(\phi, C)\nabla\left(\frac{\delta\bar{F}[\phi, C, T]}{\delta C}\right) + \eta(\vec{x}, t) \tag{20}$$

where solute mobility $M(\phi, C) = \frac{v_m}{RT_A} D_L q(\phi) C(1-C)$ and $q(\phi)$ is a function that interpolates between solid and liquid diffusivities ($q(0) = 1, q(1) = q^- = D_S/D_L$). When temperature variations cannot be neglected, an additional variational equation for the evolution of T can be included.[38] For many practical cases the diffusion of solute is several orders of magnitude slower than thermal diffusion, and it is reasonable to neglect spatial variations of temperature. As in the case of the order parameter, the noise term in Eq. (20) describes thermal-induced fluctuations in concentration. In the simulations presented in this paper, noise has been neglected.

The above alloy phase-field model can also be extended to the simulate directional solidification. The simplest way to model this process is to consider pulling an alloy sample through a temperature gradient G at a speed V. Since the ratio of thermal to chemical diffusivity is typically $\approx 10^4$ in alloys, the temperature field can be approximated by its quasi-static steady state solution $T = T_o + G(z - Vt)$[3,14,15,37] where z measures the distance along the growth direction from a reference point where the temperature $T = T_o$. Expressing temperature in units of $m_L(1-k)C_o^l$, where C_o^l is the initial alloy concentration, the temperature dependence in the free energy can be substituted by the term

$$\theta = (1-k)(z - Vt)/l_T \tag{21}$$

where $l_T = m_L(1-k)C_o^l/G$ is the thermal length, a characteristic length scale that sets the freezing range of the alloy. We will show below that l_T, the capillary length (d_o) and the solute diffusion length ($l_D = 2D_L/V$), set the scaling of primary dendrite spacing selection in directional solidification.

3.2.1. *Sharp-interface limit of phase-field models*

When the diffusion length is much greater than the nano-scale solid-liquid interface, phase-field simulations must recover the physics of the sharp interface model described in the previous section. This is done by asymptotically matching the solutions of Eqs. (18) and (19) inside and outside a thin boundary layer defined by the length scale W_o.[17,18,26,28,36] Specifically, the inner solutions of ϕ and C are expanded in some small parameter and matched (order by order) to their outer counterparts in such a way that the following three conditions are satisfied:

(1) the dynamics outside the interface region are governed by the diffusion equation, with appropriate diffusion coefficients in each phase,
(2) the interface concentration of the outer C-field satisfies the Gibbs–Thomson condition,
(3) the derivatives of the outer C-field, evaluated on either side of the interface, satisfy flux conservation.

Asymptotic analysis is similar in all its variants,[17,18,20,26,28,36] but the specific outcomes depend on such details as the choice of small parameter(s), the scaling of the equations of motion, the order of the expansion and the ratio of solid-liquid diffusivities. We present here the results of a new analysis, which is based on the following assumptions and procedures: We rescale the inner region of Eqs. (18) and (19) by W_o and the outer region by D_L/V_c, where $V_c = D_L/d_o$ is a characteristic speed of diffusing across scales of order the capillary length. Time is also rescaled, in both inner and outer regions, by D_L/V_c^2. The inner and outer ϕ and C fields are expanded in the small parameter $\epsilon_1 = W_o/d_o$, after which an order by order matching of the inner and outer solutions of Eqs. (18) and (19) is performed (up to order ϵ_1^2, and to first order in the small parameter $\epsilon_2 = W_o\kappa$). This yields the following sharp interface limit of Eqs. (18) and (19):

(1) Diffusion in bulk phases

$$\partial_t C = D_{S,L}\nabla^2 C$$

(2) Flux conservation across interface:

$$D_S \nabla C\cdot\vec{n}|_S - D_L\nabla C\cdot\vec{n}|_L = \Delta C_o V_n + \Delta H V_n W_o\kappa + \Delta J\partial_\theta(\kappa\partial_\theta\mu)W_o\kappa$$

(3) Local Interface concentrations ($C^\pm$):

$$\delta C = -\frac{(\sigma_\phi + \bar{r}\sigma_c)W_o\Lambda}{d_\mu\Delta C_o}\kappa - \frac{\tau_o\Lambda}{W_o}\left(1-\frac{\gamma}{\bar{D}\Lambda}\right)\frac{\sigma_\phi}{d_\mu\Delta C_o}V_n$$

where $D_{S,L}$ denotes the solid/liquid diffusivities, $\delta C = C^\pm - C_L$ with $C_{L,S}$ the equilibrium solid/liquid interface concentrations, $\Delta C_o = C_L - C_S$, $\bar{r} = (W_c/W_o)^2$, $\vec{n}$ is the local interface normal, V_n the local interface velocity, $\bar{D} = D_L\tau_o/W_o^2$ and $d\mu \equiv \partial_C\mu|_{C_L}$. Other constants are defined as: $\sigma_\phi = \int_{-\infty}^{\infty}(\partial_x\phi_o)^2dx$ and $\sigma_c = \int_{-\infty}^{\infty}(\partial_x C_o)^2dx$, where the field C_o is the equilibrium concentration profile (obtained by solving

$$\partial_{CC}\bar{f}_{AB} - \Lambda\bar{r}\partial_{xx}C_o = \mu_{\rm eq} \tag{22}$$

for C_o). The field ϕ_o solves the lowest order phase-field equation $\partial_{xx}\phi_o - dg(\phi_o)/d\phi = 0$. Finally, $\gamma = (K + \Delta C_o F^\pm)/\sigma_\phi$, with the constants K, ΔF, ΔH and ΔJ defined by

$$K = \int_{-\infty}^{\infty}\frac{\partial C_o}{\partial x}\left(\int_0^\xi \frac{(C_o(x')-C_S)}{Q(\phi_o,C_o)}dx'\right)dx$$

$$\Delta F = \left[\int_0^\infty \frac{\Delta C_o}{C_L(1-C_L)} - \frac{(C_o-C_S)}{Q(C_o,\phi_o)}dx\right] - \left[\int_{-\infty}^0 \frac{(C_o-C_S)}{Q(C_o,\phi_o)}dx\right]$$

$$\Delta H = \int_0^\infty (C_L - C_o)dx - \int_{-\infty}^0 (C_o - C_S)dx$$

$$\Delta J = \int_0^\infty (Q(C_L,0) - Q(C_o,\phi_o))dx - \int_{-\infty}^0 (Q(C_o,\phi_o) - Q(C_S,1))dx$$

where $Q(C_o, \phi_o) \equiv C_o(1 - C_o)q(\phi_o)$ and where F^+ and F^- are defined by the first and second large square brackets of the ΔF equation. The "0" lower limit in the above integrals corresponds to the interface location, which, following Ref. 17, we define by the level set where $\phi(\vec{x}, t) = C_i$, where $0 < C_i < 1$. The variable θ is the arc length along the interface.

The sharp interface limit of the phase-field model contains three so-called *corrections* terms: ΔF (solute trapping), ΔH (interface stretching) and ΔJ (interface diffusion). These emerge in all phase-field models where the solid and liquid diffusivities are different.[26,28] The ΔJ term can essentially be neglected (or is at least bounded), since for most solidification structures $W_o\kappa \ll 1$. The ΔF and ΔH terms, however, are velocity-dependent, and become greatly amplified in the limit $W_o \gg d_o$, which is numerically important to avoid unnecessary mesh refinement and to decrease simulation times (even up to quite large undercooling). It is straightforward to show that both ΔH and ΔF can easily be made to vanish by appropriate choices of (1) diffusivity function $q(\phi)$ and (2) interface level set definition C_i.

3.2.2. *Non-variational approach*

At low undercooling, the only way to simulate experimentally relevant microstructure sizes, in reasonable time, is to (1) operate the phase-field model with an *extremely* diffuse interfaces W_o and (2) use adaptive-mesh refinement (see Sec. 4). In this limit, all three correction terms above become sizable and must be made to vanish. It is exceedingly difficult (though not impossible) to simultaneously set all three correction terms to zero using the thermodynamically consistent phase-field formulation discussed above. An alternative approach has been developed in Refs. 26 and 36 for the particular case of the free energy in Eq. (17). In that work, the variational approach is abandoned in favor of a set of phase-field equations that are constructed to reproduce the sharp-interface limit. The methodology is summarized here.

One begins by defining a normalized chemical potential ($u = \mu - \mu_E$)

$$u = \ln\left(\frac{2C}{C_o^l[(1+k) - (1-k)g_s(\phi)]}\right) \tag{23}$$

where $g_s(\phi)$ controls entropy interpolation between $\phi = -1$ (liquid) to $\phi = 1$ (solid) in Eq. (18), and satisfies $g_s(\pm 1) = \pm 1$. (The energy interpolation function $G(\phi)$ is related to $g_s(\phi)$ such that the steady-state profile $\phi_o = -\tanh(x\sqrt{2}W_o)$.) Finally, C_o^l is the initial alloy concentration.

In terms of the u-field, the equation of motion for ϕ becomes

$$\tau(\vec{n})\frac{\partial\phi}{\partial t} = W_\phi^2(\vec{n})\nabla^2\phi + \frac{dg}{d\phi} - \frac{\lambda}{1-k}(e^u - 1)\frac{dg_s}{d\phi}(\phi)$$
$$+ W_o\frac{1}{2}\nabla\cdot\left[|\nabla\phi|^2\frac{\partial A^2(\vec{n})}{\partial(\nabla\phi)}\right] \tag{24}$$

where $\lambda = -RT_m(1-k)^2 C_o^l / v_m \Lambda$, T_m is the melting temperature and k is the partition coefficient. The first, second and fifth terms of Eq. (24) arise because the interface kinetics time and interface width are made anisotropic according to the phenomenological function $W_\phi = W_o A(\vec{n})$ and $\tau = \tau_o A(\vec{n})^2$, respectively.

Solute transport is defined by Eq. (19), with the flux $\vec{J}$ modified by a so-called *anti-trapping* current $\vec{J}_{at} = -a_t W_o C_o^l (1-k) e^u (\partial_t \phi) \vec{n}$, where a_t is a constant. The current $\vec{J}_{at}$ makes it possible to eliminate the solute trapped due to the finite thickness of W_ϕ. The choice of constant a_t (more generally, a function of ϕ), along with the choice of $g_s(\phi)$ and $q(\phi)$ provide three degrees of freedom with which to easily eliminate the constraints ΔF, ΔH and ΔJ.[26,36] The interesting feature of using the anti-trapping current is that it allows us to recover the sharp-interface limit for dilute binary alloys using the same definitions for capillary length d_o and kinetic coefficient β as those given by Eqs. (11) and (12) for the solidification of pure materials.

Most of the work on binary alloys presented in this paper is based on the dilute alloy free energy in Eq. (17), and using the asymptotic analysis in Ref. 36 to simulate the sharp-interface limit of our phase-field model. Our simulations are all performed in the limit where we can ignore interface kinetics (i.e. $\beta = 0$). (We note that spurious curvature, temperature and kinetic corrections to the kinetic coefficient have been ignored in our directional solidification simulations[26] as these were found to be fairly small). Diffusion is simulated using the interpolation function $q(\phi) = \frac{(1-\phi)}{(1+k)-(1-k)\phi} + \frac{(1+\phi)q^-}{2}$ while $d_o/W_o = a_1/\lambda$. Furthermore, setting the interface kinetics coefficient in Eq. (12) to zero gives $\frac{D_L \tau_o}{W_o^2} \approx 0.6267\lambda$. The anti-trapping coefficient $a_t = 1/(2\sqrt{2})$. In Sec. 5.3, a variational phase-field model is used, which features a free energy with parallel solidus and liquidus lines. In that case, the sharp interface limit of those simulations was attained using the new asymptotic analysis presented in this paper (Sec. 3.2.1).

Figure 6 shows a snapshot in the time evolution of the concentration field of directionally solidified SCN-0.13 wt% PVA alloy. The parameters of the simulations correspond to thermal gradient $G = 9.75$ K/mm, pulling velocity $V = 30$ μm/s (cooled bottom to top). Microsegregation is evident between dendritic branches, while coring occurs in the solid phase.

3.3. *Phase-field models in 3D including fluid flow*

The phase field methods described above can be extended to 3D with fluid flow included in the melt along with solidification.[24,41–43] We present here the case of a pure material. Since there is no phase boundary, the model must include some means for extinguishing the flow inside the solid phase. Beckermann *et al.*[43] introduced a mixture formulation for the continuity, Navier–Stokes and energy balance equations, and an auxiliary interfacial stress term into the Navier–Stokes equation to ensure that the shear stress is correct at the interface. The phase-averaged

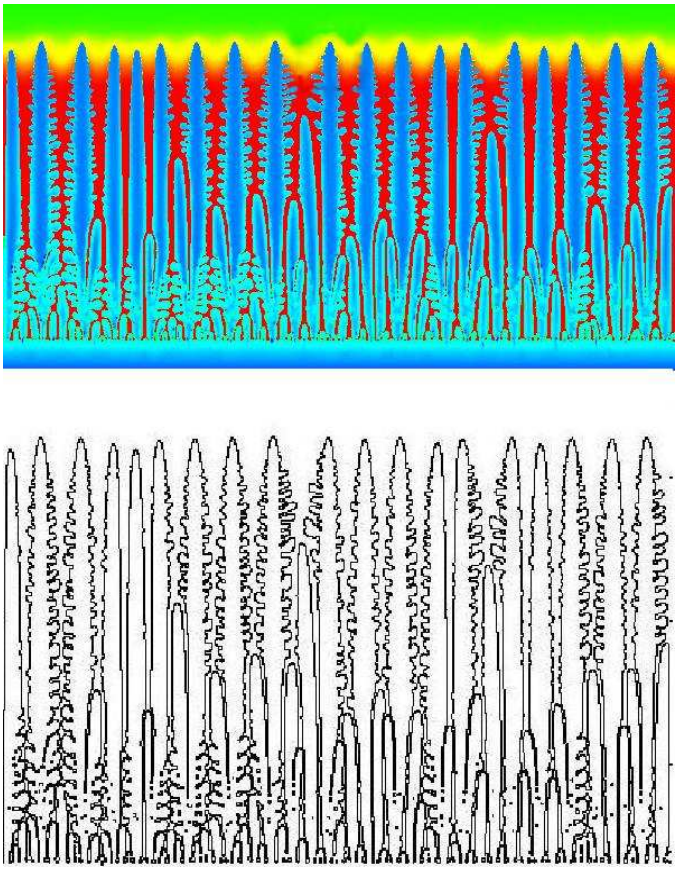

Fig. 6. Top: Directionally solidified dendrites grown at a speed $V = 30$ μm/s and a thermal gradient $G = 9.75$ K/mm. Shade of gray (color online) represents solute concentration. Lighter shades (warmer colors online) represent high concentration while darker shades (cooler colors online) represent low concentration. Bottom: The corresponding interface position, calculated by finding the level set $\phi = 0$.

mixture continuity is given by

$$\nabla \cdot \left[\frac{1-\phi}{2} \boldsymbol{v} \right] = 0 \tag{25}$$

where $\boldsymbol{v}$ is the velocity vector, and the momentum balance equation is

$$\frac{\partial}{\partial t} \left[\left(\frac{1-\phi}{2} \right) \boldsymbol{v} \right] + \left(\frac{1-\phi}{2} \right) \boldsymbol{v} \cdot \nabla \boldsymbol{v} + \left(\frac{1-\phi}{2} \right) \frac{\nabla p}{\rho_o}$$

$$= \nu \nabla^2 \left[\left(\frac{1-\phi}{2} \right) \boldsymbol{v} \right] - \nu \frac{h(1-\phi^2)(1+\phi)}{8\delta^2} \boldsymbol{v} \tag{26}$$

where t is time, p is pressure, ρ_o is the (constant) density, ν is the kinematic viscosity, $\delta = W_o/\sqrt{2}$ is the characteristic interface width, and h is a constant

(= 2.757) which ensures that the interface shear stress is correct for a simple shear flow (see Beckermann *et al.*[43]). Finally, the phase-averaged energy equation is written in terms of the scaled temperature U (see Sec. 3.1) as

$$\frac{\partial U}{\partial t} + \left(\frac{1-\phi}{2}\right)\boldsymbol{v}\cdot\nabla U = \nabla\cdot(D\nabla U) + \frac{1}{2}\frac{\partial \phi}{\partial t} \tag{27}$$

where $D = \alpha\tau_o/W_o^2$ in which α is the thermal diffusivity. W_o and τ_o have the same interpretation as they did in 2D. The 3D phase-field evolution equation is a straightforward extension of the 2D form, given by

$$\begin{aligned}\tau(\mathbf{n})\frac{\partial \phi}{\partial t} &= \nabla\cdot[W_\phi(\mathbf{n})^2\nabla\phi] + [\phi - \lambda U(1-\phi^2)](1-\phi^2)\\ &\quad + \partial_x\left(|\nabla\phi|^2 W_\phi(\mathbf{n})\frac{\partial W_\phi(\mathbf{n})}{\partial(\partial_x\phi)}\right)\\ &\quad + \partial_y\left(|\nabla\phi|^2 W_\phi(\mathbf{n})\frac{\partial W_\phi(\mathbf{n})}{\partial(\partial_y\phi)}\right)\\ &\quad + \partial_z\left(|\nabla\phi|^2 W_\phi(\mathbf{n})\frac{\partial W_\phi(\mathbf{n})}{\partial(\partial_z\phi)}\right).\end{aligned} \tag{28}$$

4. Multiscale Simulations Using Dynamic Adaptive Mesh Refinement (DAMR)

4.1. *DAMR in 2D*

A major computational challenge to simulating phase-field models efficiently involves the disparity between the interface width W_o and diffusion length scales. While careful asymptotic matching of inner and outer solutions provides recipes for increasing the ratio of W_o/d_o (thus increasing the effective kinetic time scale τ_o), several orders of magnitude still separate d_o, D/V and L_B (the system size). The main physics of solidification (and many other reaction-diffusion problems) occurs near an interface whose area is much smaller than the full computational domain. In this region, the order parameter varies significantly, while away from the interface variations in ϕ are small. Meanwhile, the diffusing field(s), denoted in this section as U, typically extends well beyond the interface and has much more gradual variation (lower gradients) throughout the entire simulation domain. A much coarser grid may be used to resolve U. The most obvious manner to overcome this inherently multiscale problem is to establish a high density of grid points where the ϕ or U fields vary most rapidly and a significantly lower grid density in other regions. To be successful, an efficient method must dynamically adapt the grid to follow the evolving interface,[30,31,46,47] while at the same time maintaining a certain level of solution quality.

This section describes methods for solving Eqs. (9) and (10) in 2D using the Galerkin finite element method on a dynamically adapting mesh of linear, mixed

isoparametric quadrilateral and triangular elements. The algorithm is easily implemented in Fortran 95 and C++, taking advantage of such advanced features as data structures, derived data types, pointers, dynamic memory allocation and modules to conveniently store, adapt and manipulate complex grids and their solution fields. Our algorithm performs functions that can be divided into two classes. The first deals with the establishment, maintenance and updating of the finite element grid, and the second with evolving ϕ and U on this grid, according to Eqs. (9) and (10). The methodology described below has also been extended to 3D phase-field simulations combined with fluid flow[24] (Sec. 4.2), and to solidification of alloys.[14,15,37] The method can also be readily extended to most reaction-diffusion problems.

4.1.1. *Dynamic adaptive mesh data structures*

The first class of functions in our algorithm maintains a grid of finite elements on a data structure known as a *quadtree*[31,48–50] which replaces the standard concept of a uniform grid as a way of representing the simulation grid. The quadtree is a tree structure with branches down to a specified level. Branches of the quadtree point to element data structures that contain information analogous to their parent element. Figure 7 illustrates the quadtree structure as well as the relation between elements at different levels of refinement.

Every node on the quadtree contains information pertaining to a 4-node isoparametric quadrilateral finite element.[51] This information includes the following:

- values of ϕ and U at the four nodes
- the nodal coordinates of the element
- the level of refinement of the element on the quadtree
- the current value of the error estimate for the element
- the element number

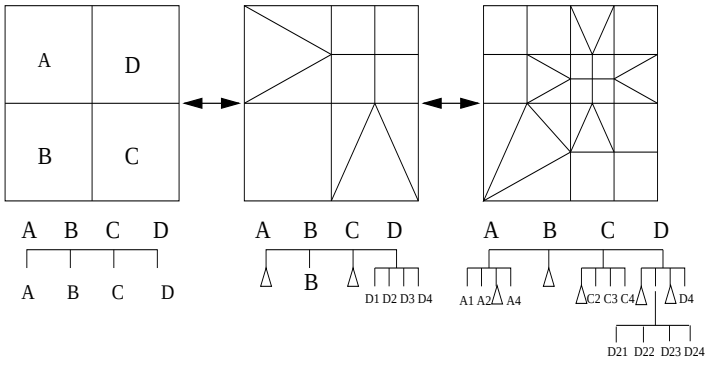

Fig. 7. An illustration of the quadtree element data structure. The first frame shows an element, and four child elements. Splitting of one of the children and one its children is shown, along with the branch evolution of the quadtree. Branches with triangles indicate square elements which are bridged with triangular or rectangular elements.

- an array mapping the element's internal node numbers onto node numbers of a global solution array
- pointers to the element's nearest neighbors sharing a common edge and at the same level of refinement
- a variable that determines whether or not an element contains further sub-elements, called *child* elements
- pointers to an element's child elements
- a pointer to the *parent* element from which an element originates.

An element of the quadtree can be refined by splitting it into four child elements, each having its own dataset. A parent element and its four child elements are referred to as a *family*. Refinement produces a finer mesh within the confines of the original parent grid by bisecting each side, as shown in Fig. 7. Unrefinement, which consists of fusing the four child elements back into the parent, has the opposite effect, locally creating a coarser mesh. Both refinement and unrefinement proceed via dynamic memory allocation and de-allocation, making storage scalable. We note that unrefinement can occur only if child elements do not possess further children of their own. Also, in order to avoid having regions of very different refinement bordering each other, we impose the restriction that any two neighboring quadrilateral elements may be separated by no more than one level of refinement (see Fig. 7). This constraint is important to maintaining solution accuracy. We define the level of refinement of an element by l_e such that a uniform grid at a refinement level l_e would contain $2^{l_e} \times 2^{l_e}$ grid points in a physical domain $L_B \times L_B$. Elements are connected to their neighbors at the same level using pointers. Cases where an element has a missing neighbor are handled using null pointers.

All elements at a given level of refinement on the quadtree are "strung" together in a linked-list of pointers, referred to as G-lists. There are as many G-lists as there are levels of refinement in the quadtree. Each pointer in the G-list points to the memory location assigned to one element node of the quadtree. The purpose of the G-list is to allow traversal of the quadrilateral elements sequentially by level, rather than by recursively traversing quadtree from the root down, a procedure which is memory intensive and very slow.

Alongside the main grid of quadtree elements, our algorithm maintains two independent linked-lists of grids representing special linear isoparametric triangular and rectangular elements. These elements are used to connect the extra "hanging" nodes that arise when two or more quadrilateral elements of differing refinement levels border each other (Fig. 7). These element types are referred to as *bridging elements*. They are maintained as two linked-lists of derived data types, one containing information about triangles and the other rectangles. Elements of both bridging element grids contain the following information:

- the values of ϕ and T at the three nodes (four for rectangles) of the element
- the nodal coordinates

- node numbers that map the element's internal nodes onto the global solution array.

The types of bridging triangles and rectangles that can occur are enumerable, as discussed in Ref. 31.

The main set of operations performed on the grids described above concern refinement of the finite element mesh. The refinement process is performed only on the quadrilateral mesh. The triangular and rectangular grids are established after this process is completed (see Fig. 7). To refine the grid, the code traverses the elements of the quadtree, refining (unrefining) any element whose error estimator, discussed below, is above (below) a critical value $\sigma_h(\sigma_l)$. We note that fusion of four quadrilateral elements is permitted only if all four of its children's error functions are below the critical value σ_l, where $\sigma_l < \sigma_h$. We note that if $\sigma_l = \sigma_h$ the grid can set into oscillations, where large numbers of elements become alternatively refined at one time step, then unrefined at the next.

The processes described thus far are grouped into modules (objects in the C++ version) that encapsulate various related tasks, and which can cross-reference each other's data and subroutines. The module highest up in the hierarchy contains the definition of the quadtree data structure. It also contains subroutines that construct the initial grid, set the initial conditions and refine/unrefine quadrilateral elements. Another module constructs the G-lists, including routines that construct the initial G-list from initial quadtree data structure, as well as add or delete subsequent element pointers from the G-list as elements are created or deleted. A third module accessing both the previous data structures creates the bridging element grids. It contains subroutines that insert triangular or rectangular elements where appropriate. These are stored in separate element linked lists.

4.1.2. *The finite element formulation*

The main program evolves ϕ and U and periodically adapts the dynamic grid. A flowchart of these processes is shown in Fig. 8.

Time integration of Eqs. (9) and (10) is performed on the dynamic adaptive grids using the finite element (FEM) method. An FEM module performs four main processes:

(1) Maps the internal element node numbers to the indices of a global solution vector. The ϕ-field is mapped onto the odd numbers, while U is stored on the even numbers of the global solution vector.
(2) Advances the U and ϕ field-vectors by M time steps on an adapted finite element grid.
(3) Calculates error estimate in quadrilateral elements.
(4) Invokes routines in the modules described above to refine the grid according to this error estimator.

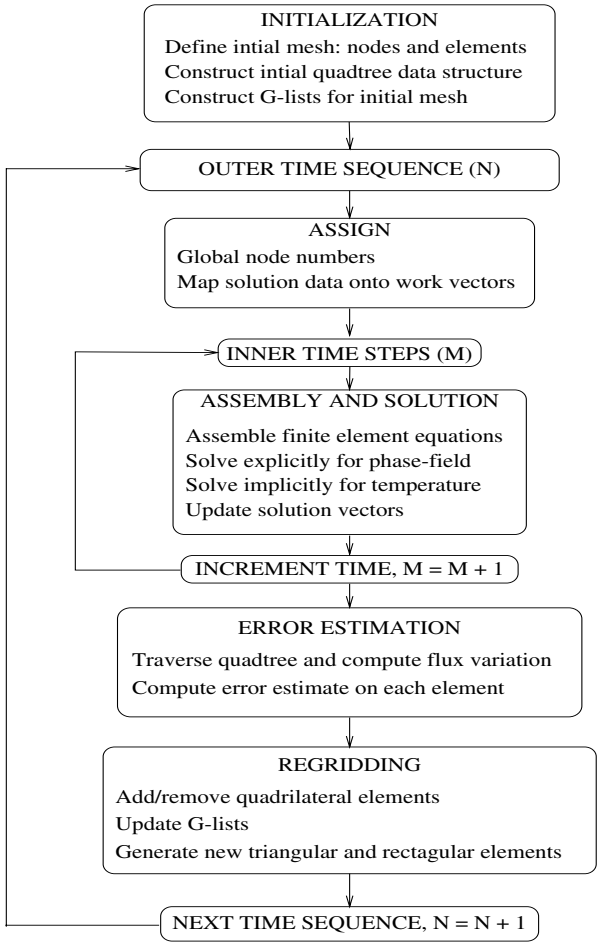

Fig. 8. Flowchart of the DAMR algorithm.

Steps (1)–(4) are repeated until a sufficient evolution of the microstructure is established. Step (1) involves searching all elements, and their neighbors, and assigning each node a unique number, which will be used to map that element node to a global solution vector. The upper limit of the variable M in Fig. 8 is dynamically chosen such that the interface (width W_o) remains entirely within the finest level of refinement. We have checked that this procedure produces essentially the same error as simulating the phase-field model on a uniform mesh corresponding to our finest level of refinement.

The finite element formulation of Eqs. (9) and (10) is done using Galerkin's weighted residual method[51] for both quadrilateral and triangular elements. Local element matrices are generated[31] using linear interpolation for both ϕ and U[52] and a lumped matrix formulation[51] is used for time derivatives to avoid matrix inversion

of the assembled global system of equations. The ϕ vector is evolved in time using a forward difference time stepping scheme. For each time step of the ϕ field, the global U field can be solved using either explicit or implicit methods.

4.1.3. *The error estimator*

Regridding is based on an error estimator function, which is obtained following Zienkiewicz and Zhu,[52] based on the differences between calculated and smoothed gradients of a weighted combination of the ϕ and U fields given by

$$\Psi = \phi + \gamma U \tag{29}$$

where γ is a constant. This is the simplest definition that allows the U and ϕ fields to contribute to the mesh refinement. The weight γ is chosen to amplify variations of the U field compared to the ϕ field. The selection of γ is discussed in more detail in Ref. 31, where it is shown that using only gradients of the ϕ-field in establishing the grid[45] can lead to large errors in calculations of tip velocity in dendritic growth. This method appropriately meshes regions of steep gradients and regions where either ϕ or U change rapidly.

Figure 9 shows a time sequence of dynamically adapting FEM gird for a directionally solidified alloy of SCN-0.13 wt% PVA. The magnification is chosen to resolve the finest levels of refinement. In the simulation, the U field of the model equations described in Sec. 3.2.2 represents the chemical potential. The sample

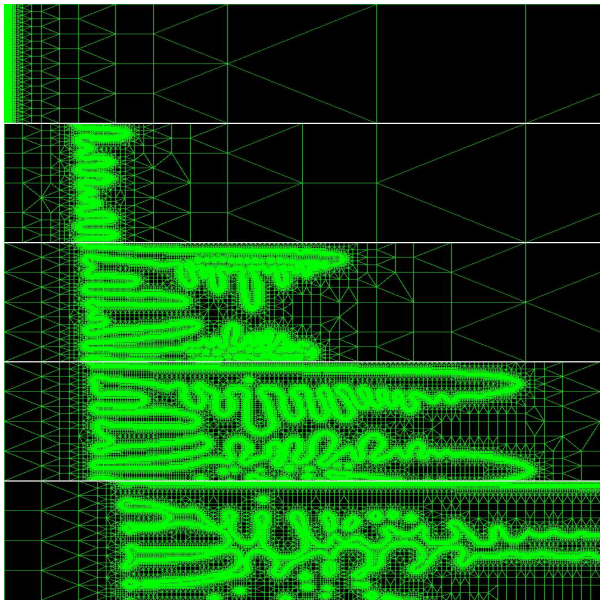

Fig. 9. Dynamic Adaptive Grid for directional solidification in a gradient $G = 9.75$ K/mm and $V = 30$ μm/s at times 0.96 s, 9.6 s, 11.5 s, 14.4 s and 29.8 s.

is being pulled through a thermal gradient of $G = 9.75$ K/mm at a speed of $V = 30$ μm/s.

4.2. *DAMR in 3D*

The need for DAMR is even more acute in 3D phase-field modeling than it is in 2D, simply because of the dimensionality. The minimum grid spacing is set by the need to resolve the interface, which must be thin compared to the diffusion length and tip radius. The size of the box is again set by the need to contain the entire diffusion field. Thus, the scale requirements affect each dimension equally, and the number of grid points in a fixed mesh scales as $(L_B/\Delta x)^d$, where d is the dimensionality.

As in 2D calculations, the grid is adapted such that it is finest in the vicinity of the interface, and coarser far away, where all of the primitive fields vary slowly. The typical ratio of largest to smallest element size is 512, but there is no inherent limit. Element refinement and fusion is done based on the value of an error estimator, computed from the solution within each element, and described further below.

The data structure in 3D is similar to that used in 2D, with the defined data types being augmented for the increased dimension and the new variables associated with the flow $(\boldsymbol{v}, p)$. The basic element is a cube, and refinement is done by bisection of each face, leading to eight child elements derived from the parent. The elements are stored on an *octree*, a straightforward extension of the quadtree used in 2D.

The grid is locally adapted based on an element-by-element error estimate, following a hybrid scheme using the magnitude of ϕ and the inter-element variation of the derivatives of U. If an element contains the interface, indicated by the condition

$$\phi_{\min} \leq \phi \leq \phi_{\max} \tag{30}$$

then the element is continuously divided until its refinement level is maximal. We found that using $\phi_{\min} = -0.99$ and $\phi_{\max} = 0.9$ gave consistent results. The reason for the asymmetry is that the interface typically moves from the solid region $\phi > 0$ to the liquid region $\phi < 0$. Outside of the interface region ($\phi < \phi_{\min}$ or $\phi > \phi_{\max}$), we used an error estimator based on the magnitudes of the derivatives of U as follows:

$$E_e = \int_{\Omega_e} \nabla U \cdot \nabla U d\Omega \tag{31}$$

where Ω_e is the element.

The grid refinement procedure begins by noting the refinement level of each element, and its immediate neighbors. Refinement is required in an element whenever the estimated error exceeds the limit value, or when the absolute difference between the refinement level of an element and that of its neighbors exceeds one. Refinement is carried out successively at each refinement level, beginning with the minimum, according to the procedure illustrated in Fig. 10. Unrefinement procedure is accomplished by fusing child elements back into the parent element, when the error estimate is sufficiently small in all of the children, as we did in 2D.

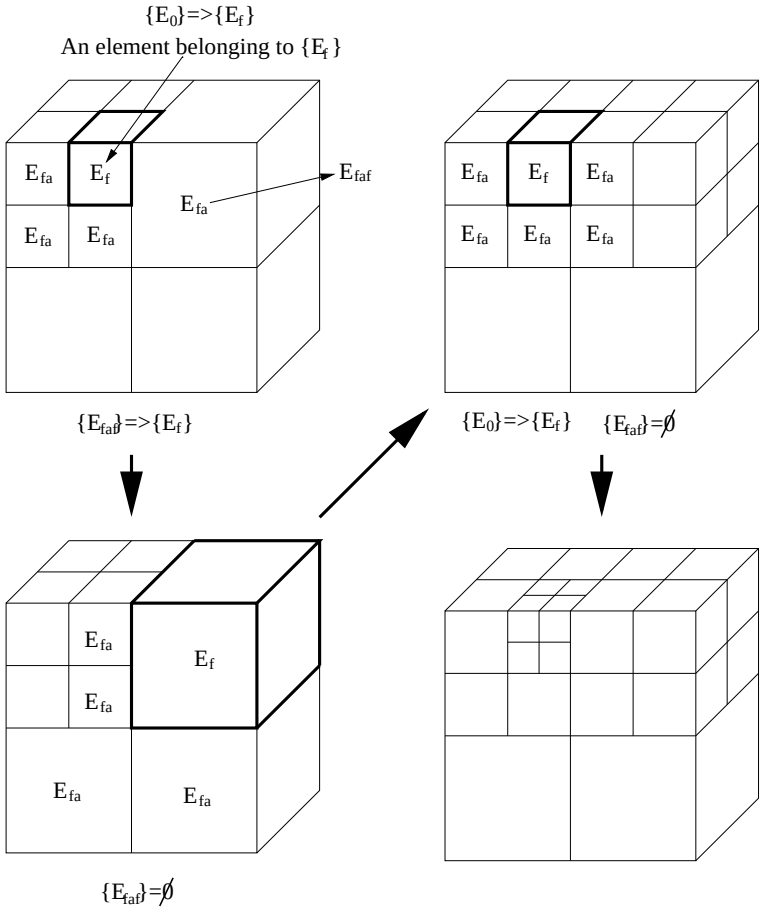

Fig. 10. Dividing sequence for refinement. The arrows indicate the sequence of refinement. (Symbols are described in detail in Ref. 24.)

Disconnected nodes appear whenever an element has a neighbor whose refinement level differs by one, as illustrated in Fig. 11. An element with connectivity 1–6, 12, 13 contacts two neighbor elements of lower refinement level. Rather than completing the mesh with special elements as we did in 2D, we instead impose constraints on the disconnected nodes. For any degree of freedom ψ_i, the constraints are

- Disconnected edge mid-nodes:

$$\psi_2 = \frac{\psi_1 + \psi_7}{2}, \qquad \psi_5 = \frac{\psi_1 + \psi_{11}}{2}, \qquad \psi_6 = \frac{\psi_1 + \psi_9}{2}. \tag{32}$$

- Disconnected face mid-nodes:

$$\psi_3 = \frac{\psi_1 + \psi_7 + \psi_8 + \psi_9}{4}, \qquad \psi_4 = \frac{\psi_1 + \psi_{11} + \psi_{10} + \psi_9}{4}. \tag{33}$$

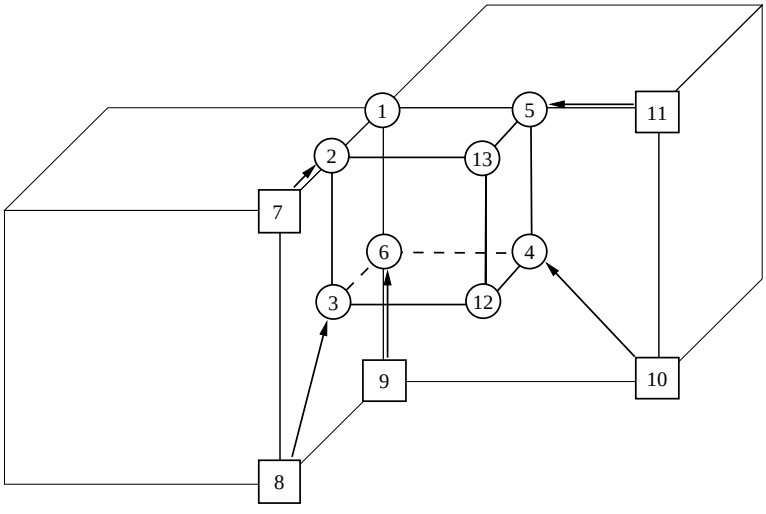

Fig. 11. Configurations of disconnected sides and nodes.

After applying the constraints, the original element connectivity is modified to be modes 1, 7–13, and the element shape functions are changed appropriately. Thus, nodes 3, 4, and 6 would be compressed out of the final calculations. This facilitates domain decomposition in the parallel implementation.

We solve Eqs. (25) and (26) via the Semi-Implicit Approximate Projection algorithm,[44] a predictor-corrector method. For a detailed discussion of the algorithm, the reader is referred to the original paper,[44] and for a detailed description of the parallel adaptive finite element implementation, see Jeong *et al.*[24]

The flow and energy balance equations are solved in an implicit, segregated fashion, whereas the phase-field equation is integrated explicitly. Different time step sizes are used for the various equations. The phase-field and energy balance equations are solved using the minimum time step, $\Delta t_{\theta\phi}$, and the fluid flow equations are solved using a larger time step Δt_v. The physical basis for this choice is that the interface moves very slowly relative to the fluid, and thus the motion of the interface does not strongly affect the flow field.

4.2.1. *Scalability and parallel computing*

Both the 2D and 3D adaptive mesh algorithms exploit the scalability attainable in physical problems where the ratio of interface area to system volume is low, such as solidification or other boundary-layer problems (e.g. combustion-front evolution).[45] The structure of our mesh data structure is easily amenable to shared memory and distributed parallelization. Figure 12 illustrates the scalability of a portable OpenMP version of our 2D alloy code across multiple processors of a 32-node shared memory Silicon Graphics computer and a DEC-HP Alpha Clus-

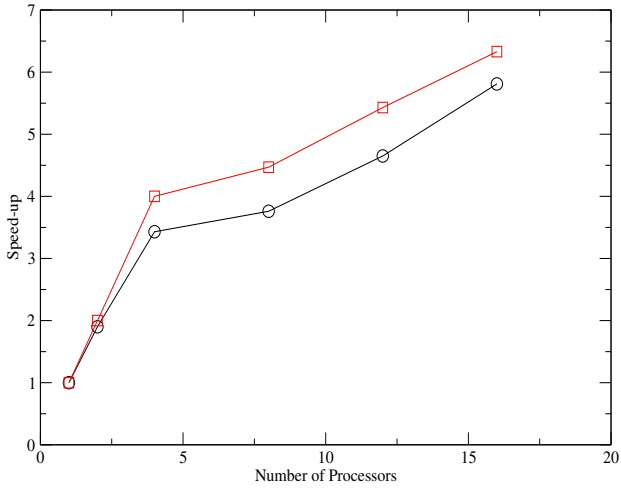

Fig. 12. CPU time versus number of processors for a simulation of a 2D directionally solidified alloy. Top curve: 32-node SGI machine. Bottom curves: 128 DEC-HP Alpha cluster.

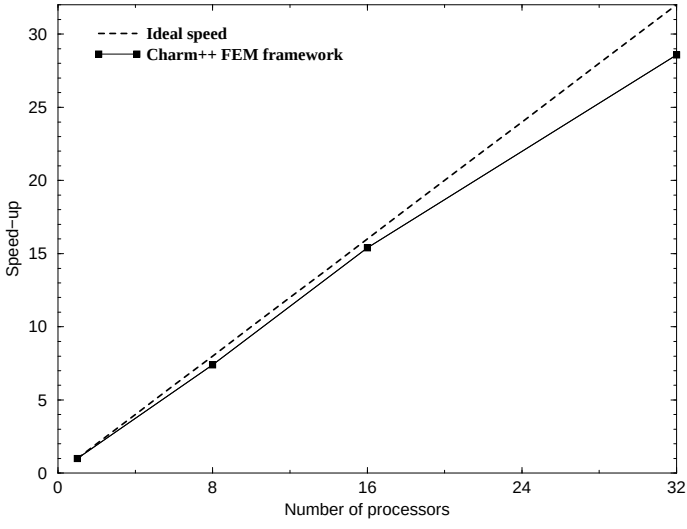

Fig. 13. Speed-up for Charm++ FEM framework for 3D solidification code.

ter. The simulation is for a directionally solidified system similar to that shown in Fig. 9.

The 3D code for pure materials was parallelized using Charm++, a message-passing parallel runtime system for machines from clusters of workstations to tightly-coupled symmetric multi-processing machines.[53] Charm++ provides a framework for the parallelization of tasks, including domain decomposition, assignment of elements to specific processors, and resolving contributions to nodes

which appear on more than one processor.[54] An example of the parallel performance of the code is shown in Fig. 13, where we used a grid with 296,636 elements and 349,704 nodes computing over 20 time steps. The value SP = 28.8 for 32 processors is typical for our code, and shows that the code has been effectively parallelized.

5. Microstructure Selection in 2D

5.1. *Dendritic growth in pure materials*

Understanding dendritic solidification has been the topic of intense investigation in recent years. Since solidification in metals is difficult to study *in situ*, much of the study of dendritic growth has focused on transparent organic analogues of metals such as alloys of succinonitrile and pivalic acid. These alloys are attractive because they solidify near room temperature and their properties are such that the solidification morphologies are similar to metals.

Early research in dendritic solidification modeling examined the properties of the sharp-interface model, both for pure materials and alloys at low undercooling. A major triumph of this research is embodied in *microscopic solvability theory*. This theory predicted both the steady state tip velocity and the radius of curvature of and isolated dendrite growing into an infinite undercooled melt. Solvability theory demonstrated that the surface tension is a singular perturbation to the Ivantsov problem (i.e. the sharp-interface model without surface tension and interface kinetics).[55] Anisotropy in the surface tension γ or interface kinetics β gives rise to an eigenvalue problem, which has solutions only for a discrete set of dendrite tip velocities and corresponding tip radii. Linear stability analysis of these steady-state dendritic solutions reveals that only dendrites with the largest allowable velocity (smallest tip radius) of this set are stable.[56–59] With the advent of new asymptotic analysis that allowed a higher order matching of simple phase-field models with appropriate sharp interface models, the theory of solvability was independently confirmed using a phase-field model of solidification.[18]

At low undercooling the diffusion of heat (pure materials) or impurities (alloy) occurs over a length scale that increases with decreasing undercooling (or supersaturation in the case of solutal dendrites). In this limit the approach to steady state follows a long-lived transient behavior, during which dendritic growth is controlled by interactions of dendritic branches with each other or with the boundaries of their container.[30,60] The study of this limit is prohibitive numerically using any fixed-grid approaches. The disparity of length scales between the diffusion length and the interface width necessitates the use of dynamical AMR techniques. Figure 14 shows DAMR simulations of the dimensionless tip speed (Vd_o/D) versus dimensionless time (t/τ_o) for thermal dendrites grown in the limit of low undercooling.

Such transient dynamics at low undercooling are characteristic of competitive interactions that occur in complex solidification problems.[24,47,56,57,60–65] In this regime, the diffusion field can be modeled by solving the heat equation in the quasi-static limit at each time step in the time evolution of the phase-field. The

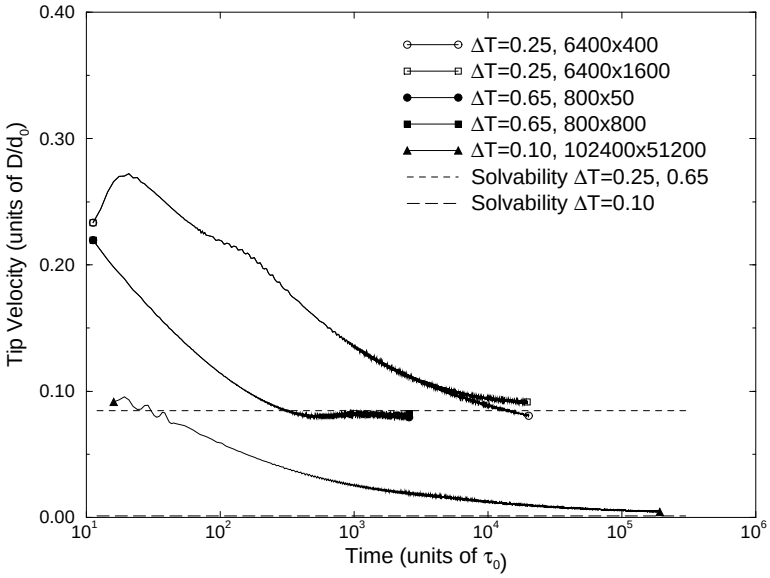

Fig. 14. Steady-state growth speed of 2D thermal dendrites (curves) at different undercooling. The horizontal lines show the predictions of solvability theory. The scales are logarithmic. ΔT refers to the dimensionless undercooling. System dimensions are also shown.

dynamics of dendritic growth in the presence of long-range diffusion interactions can be defined using the concepts of crossover scaling theory. Specifically, by rescaling the transverse dendritic growth direction as

$$y_N = \frac{y}{y_{\max}} \tag{34}$$

where $y_{\max}$ is maximum width of the dendrite arm from its center line, and the normalized dendritic arm length by

$$x_N = \frac{x - x_{\text{root}}}{x_{\text{tip}} - x_{\text{root}}} \tag{35}$$

where x_{root} defines the base of the dendrite where it emerges from the seed nucleus, the dendrite arm morphology has been shown to follow a similarity solution. Figure 15 shows morphological scaling obtained by collapsing multiple time sequences of simulated 2D and 3D dendrites onto one dendrite similarity solution.[66] The simulations do not have noise and thus do not exhibit sidebranches. We expect the scaling of the primary branch shape to remain unchanged in the presence of noise. Superimposed on the computed results is a scaled time sequence of PVA dendrites grown in microgravity.[66]

The transient growth of the dendrite arm along directions parallel and transverse to the tip have been found to obey power-law scaling of the form $v \sim t^{\alpha}$, where $\alpha \approx 0.5$ in the transverse direction and $\alpha \approx 0.78$ in the growth direction at early time, crossing over to $\alpha \approx 1$ at late times.[66] The data in Fig. 15 simulate dendritic growth for the case with zero flux diffusional boundary conditions. Changing

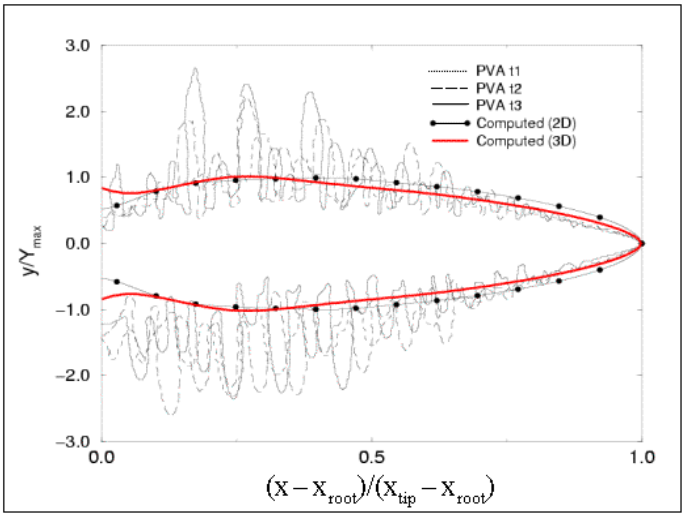

Fig. 15. Dynamic scaling of computed 2D and 3D dendritic crystal morphology using the DAMR technique. The figure also contains experimental PVA dendrite arms scaled at different times (see Ref. 66).

the assumptions of the boundary conditions or analyzing only the dendritic tip in isolation will give different growth exponents[33,67] for the same scaling regime. The remarkable feature of the data in Fig. 15 is that it predicts the universal scaling of morphology and growth rate of dendrites in the "Laplacian" limit (i.e. at low under cooling).

5.2. *Spacing selection in directional solidification of dilute binary alloys*

The role of inter-dendritic interactions is most important in casting where multiple dendrites compete to establish the final length scale of solidification microstructures. In the solidification of a binary alloy the interaction of impurity solute fields is coupled to the driving force provided by thermal gradients. An important experimental tool for studying microstructure development is directional solidification using transparent organic alloys directionally solidified at a constant velocity through a fixed temperature gradient. The interplay of temperature gradient and alloy composition lead to a complex dependence of the inter-dendritic spacing on the experimental parameters.[68–75] Recent phase-field simulations using adaptive-mesh refinement have enabled the examination of scaling in spacing selection in directional solidification of PVA-ACE and SCN-ACE systems at experimentally relevant parameters.[37] Quantitative agreement between simulation and experiments is made possible by using the alloy phase-field models described in Sec. 3.2.2 (e.g. a corrective anti-trapping current has be added to eliminate spurious solute trapping[36]).

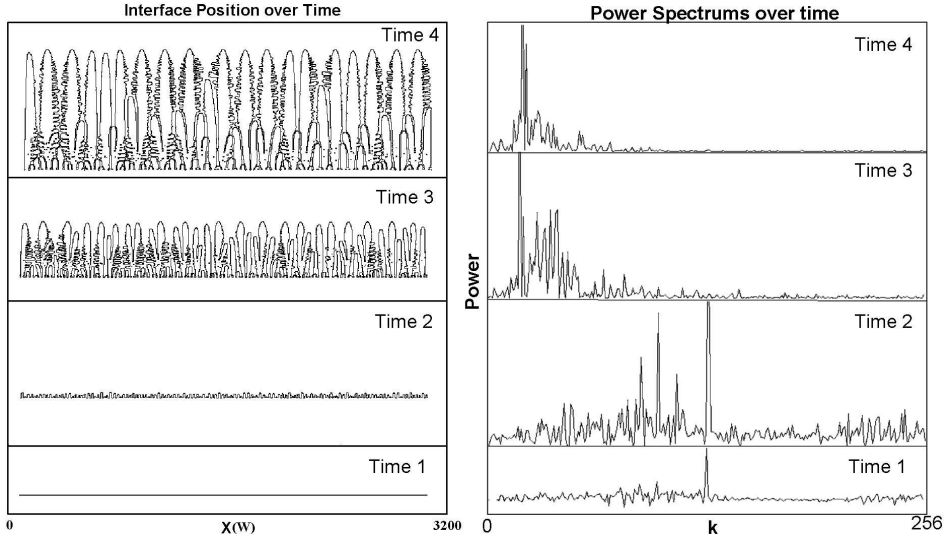

Fig. 16. (Lleft) Typical solid-liquid interface of a dendritic array directionally cooled at a pulling speed of $V_s = 150$ μm/s through a temperature gradient $G = 1500$ K/mm. (Right) The corresponding power spectrum of the interfaces on the left, showing the rapid establishment of the primary inter-dendritic spacing, identified by the peak wave vector k_{mean}. Units of length are all in the phase-field interface width W_o.

In order to address the issues of length scale selection in directional solidification, we must first determine a method to describe microstructure quantitatively. Greenwood *et al.*[37] examined the shape of the solid-liquid interface using power spectrum analysis. Following Jasnow and Vinals,[76] the primary branch spacing λ_1 was identified by the mean of the power spectrum $P_k = \langle |h_k|^2 \rangle$, where $k = 2\pi/\lambda$ is the wavevector corresponding to length scale λ and $h(z)$ represents the interface profile (made monotonic by following the contours of the dendritic envelopes). In all cases the main peak wavevector of P_k (denoted k_{mean}) corresponds to the visually observed primary spacing λ_1. The value k_{mean} was plotted versus $1/t$ and extrapolated to infinite time to obtain an estimate of λ_1. The time evolution of a typical dendritic array and its corresponding power spectrum are shown in Fig. 16.

Simulations were carried out for three sets of phase-field parameters (see Ref. 37): (G, λ, C_o^l, k): (0.00191, 20, 0.13 mol%, 0.16), (0.0015, 3, 1.5 mol%, 0.15), and (0.002, 1.3, 1.5 mol%, 0.15), where G is the dimensionless thermal gradient, λ is the coupling coefficient, C_o^ℓ is the alloy composition and k is the alloy partition coefficient. Setting the liquid diffusivity $D_L = 6.0 \times 10^{-10}$ m^2/s and the capillary length $d_o = 2.12 \times 10^{-8}$ m, (appropriate for PVA-ACE), the interface width W_o and interface kinetics time τ_o are given by $W_o = (4.0 \times 10^{-7}$ m; 6.05×10^{-8} m; 3.1×10^{-8} m), and $\tau_o = (3.3 \times 10^{-3}$ s; 1.14×10^{-5} s; 1.3×10^{-6} s), respectively. These parameter inter-relationships are set by the phase-field asymptotics in Ref. 36. As the pulling velocity V_p was varied we observed cellular structures at low values of V_p, while

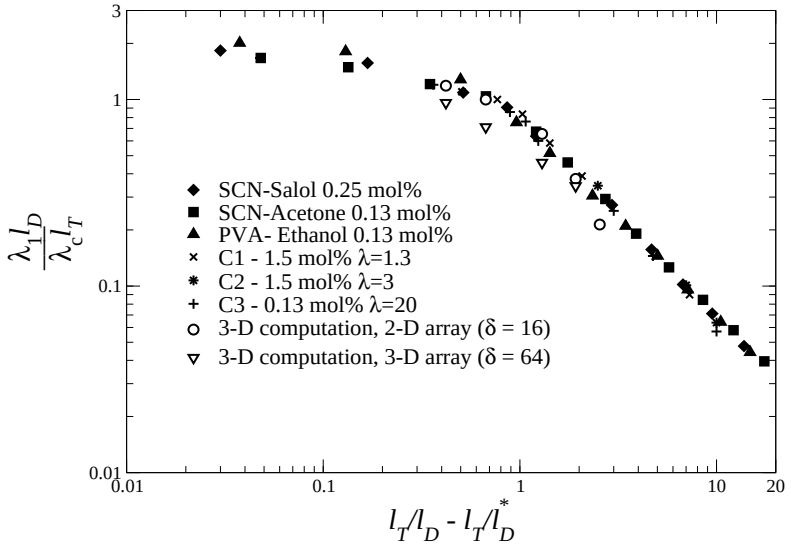

Fig. 17. Dendrite spacings from computations and experiments or Ref. 72 scaled to material properties, producing a single scaling function for primary spacings λ_1.

at high velocities we observed the emergence of dendritic morphologies. For all our simulation data a maximum occurs in λ_1 as V_p approaches the planar-cellular onset. In particular, we found that this maximum value occurs at V_p^* where $l_T \approx l_D$, where l_T and l_D are the thermal and diffusion lengths, respectively. The presence of such a maximum has been predicted theoretically[77] and observed in experiments.[69,72]

Figure 17 shows our simulation data collapsed onto a plot of dimensionless wavelength versus a dimensionless velocity. On the same plot are superimposed three experimental data sets taken from Ref. 72. The three experiments in Fig. 17 are for SCN-0.25 mol% Salol at 13 K/mm, SCN-0.13 mol% ACE at $G = 13$ K/mm and PVA-0.13 mol% Ethanol at $G = 18.5$ K/mm. The change in the two slopes corresponds to $V_p = V_p^*$, where the raw data exhibit a peak in the wavelength versus pulling velocity. Figure 17 shows primary branch selection can be described by a crossover scaling function of the form

$$\frac{\lambda_1}{\lambda_c} = \frac{l_T}{l_D} f\left(\frac{l_T}{l_D} - \frac{l_T}{l_D^*}\right) \tag{36}$$

where λ_c is the onset steady state wavelength at the transition from the planar-to-cellular instability and $l_D^* \equiv 2D/V_c$, where V_c is the velocity at the onset from planar to cellular solidification. The data in Fig. 17 are remarkable in that they show a single scaling function describing the primary spacing (λ_1) versus velocity over a wide range of pulling speeds, thermal gradients and alloy concentrations. The crossover function in Fig. 17 covers the regime from cellular fingers and crosses over into the dendritic regime. Figure 17 also includes data from 3D simulations, described in the next section.

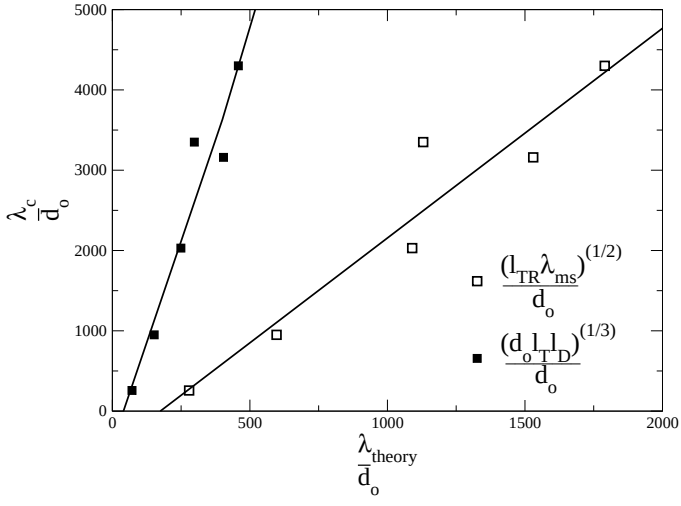

Fig. 18. A plot of λ_c/d_o versus $\sqrt{\lambda_{\rm ms} l_{\rm TR}(V_c)}$ (lower line), and $(d_o l_D l_T)^{\frac{1}{3}}/d_o$ (steeper line).

The critical onset wavelength λ_c in the scaling collapse can be compared to theoretical predictions. Specifically, Fig. 18 compares our values of λ_c to $\lambda_{\rm theory} = \sqrt{\lambda_{\rm ms} l_{\rm TR}(V_p = V_c)}$, where $\lambda_{\rm ms}$ denotes the usual Mullins–Sekerka wavelength at the planar-to-cellular onset boundary[3] (i.e. where $V_p = V_c$), and $l_{\rm TR}(V_p)$ is a velocity-dependent generalization of l_T, implicitly determined from

$$l_{\rm TR} = l_T \left(1 - \exp\left(\frac{-l_{\rm TR} V_p}{D}\right)\right) . \tag{37}$$

Physically, $l_{\rm TR}(V_p)$ is proportional to the amplitude of cellular fingers and satisfies $l_{\rm TR} \approx l_T(1 - l_D^*/(2l_T))$ at the onset of cellular growth, while in the limit $(V_p \gg V_c)$, $l_{\rm TR} \to l_T$. This form of $\lambda_{\rm theory}$ is similar to a previous analytical prediction of λ_c derived geometrically by approximating the tip shape and calculating the tip undercooling.[77] In the same figure we compare our extracted numerically λ_c to a second prediction, $\lambda_{\rm theory} = (d_o l_D l_T)^{\frac{1}{3}}$, which represents the geometric mean of the three length scales, empirically suggested to be proportional to the wavelength at the planar-to-cellular onset.[70] Figure 18 suggests that for both cases $\lambda_c = \alpha\lambda_{\rm theory}(1 + \beta d_o/\lambda_{\rm theory})$, where α and β are material independent constants. Our data show that our extracted λ_c is consistent with both theoretical predictions within a correction term that depends in a non-trivial way on surface tension.

5.3. *Misorientation of crystal anisotropy and thermal gradient: Seaweed structures*

Another class of directionally solidified microstructures is known as *seaweed*.[15,75,78,79] These structures are formed through successive tip splitting of the primary branches of a directionally solidified front. Surviving tips grow and

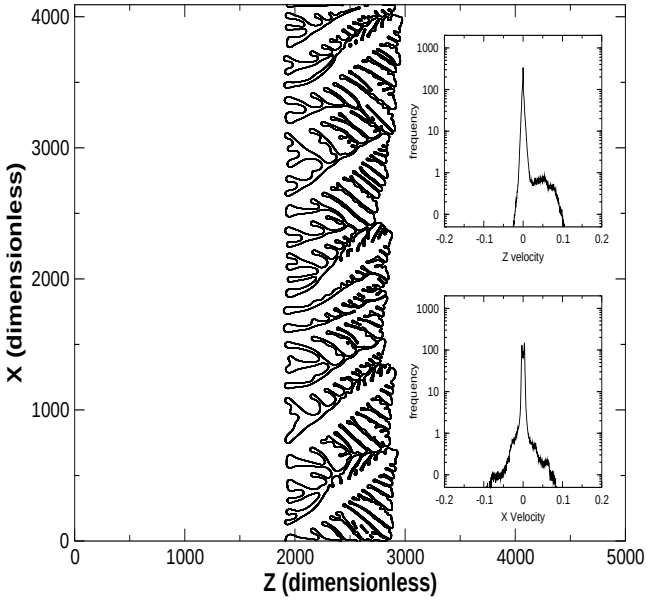

Fig. 19. Directional solidification with the surface tension anisotropy oriented at 45° with respect to the z-axis. $G = 0.8$ k/mm and $V_p = 32$ μm/s. Below a critical thermal gradient (oriented along the z-axis) the surface tension anisotropy controls the growth and dendritic structures emerge, oriented very closely the 45° axis. The insets show the velocity distribution in the x and z directions, respectively.

continue to split, while trailing branches become subsumed by neighbor interactions. Seaweeds can emerge when the temperature gradient is misoriented with respect to the preferred growth direction corresponding to the minimum in surface tension. It is brought about by a competition between the driving force provided by the thermal gradient and the lower free energy along the axis of surface tension anisotropy. Figures 19 and 20 show the morphological transition of a directionally solidified front that occurs as the thermal gradient G is increased from zero to above some critical value. In Fig. 19 surface tension anisotropy controls the minimization of free energy, which results in dendritic crystals oriented in the direction of the surface tension anisotropy (45° with respect to the z-axis). In Fig. 20, the thermal gradient (i.e. driving force along z-direction) is increased and a competition sets in between the preferential direction of surface tension anisotropy and the cooling direction. The ensuing competition leads to the characteristic seaweed-like structures evident in Fig. 20.

The morphological change from dendrites to seaweed can characterizing the distribution of local interface velocities.[15] The inset of Fig. 20 shows a sharp velocity distribution typical of seaweeds, while a broadening characterizes the distribution as dendrites emerge (insets of Fig. 19). For the parameters in Figs. 19 and 20, the

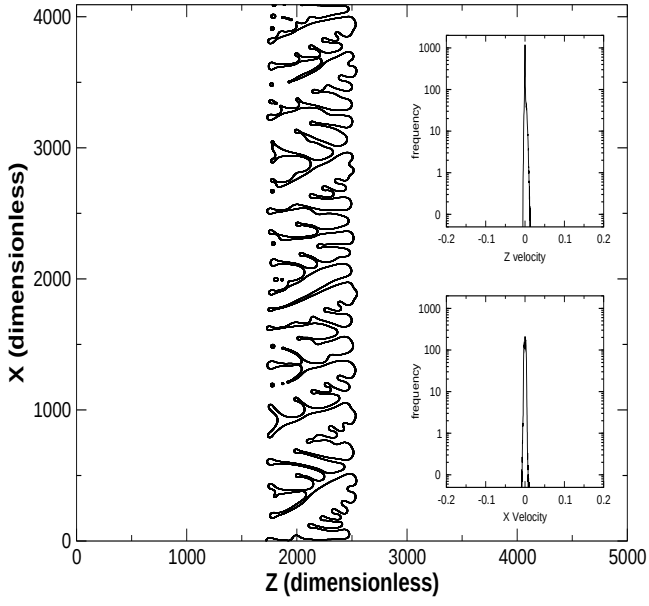

Fig. 20. Directional solidification with the surface tension anisotropy oriented at 45° with respect to the z-axis. Parameters are the same is in Fig. 19. As the thermal gradient increases a competition between growth in the forward direction and the direction of surface tension anisotropy leads to multiple dendritic tip splittings, and a subsequent crystal structure that resembles seaweed. The insets show the velocity distribution in the x and z directions, respectively.

morphological transition from seaweeds to dendrites can be approximated[15] by

$$G^* \approx P_f \sqrt{(V_p \cos\theta)/(D d_o(1 + 15\epsilon_4 \cos 4\theta))} \tag{38}$$

where $P_f = 0.004$, V_p is the pulling velocity, θ is the angle of anisotropy, D is the diffusion constant, d_o is the capillary length and ϵ_4 is the anisotropy strength. This selection criterion defines a morphological phase diagram in $V_p - G$ space for a fixed ϵ_4, predicting a crossover from seaweed to oriented dendrites as V_p increases. At sufficiently large V_p we still expect the fastest growing unstable wavelength to occur in the forward direction regardless of the angle of anisotropy. We therefore only expect Eq. (38) to hold for small V_p.

6. Dendritic Growth in 3D

In this section, we discuss 3D dendritic growth in the presence of fluid flow using a phase-field model coupled to fluid flow and solved with the 3D DAMR algorithm. For further details, the reader is referred to the original papers.[24,80,81] The extension to 3D was motivated in part by the desire to study the effect of fluid flow on the evolution of microstructure. The mechanism by which the flow alters the solidification process is by transport of heat or solute from the leading edge to the trailing edge of the growing dendrite.[82] The process is illustrated schematically in

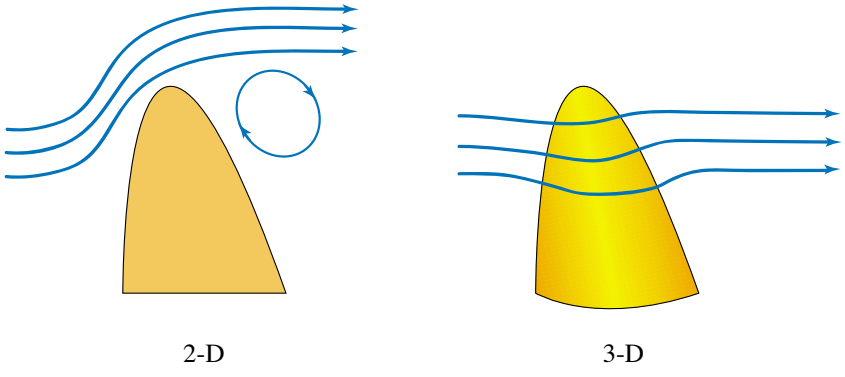

Fig. 21. Comparison of advective transport mechanisms in 2D and 3D for dendritic growth.

Fig. 21, where one can clearly see that the process works fundamentally differently in 3D, where heat or solute is easily transferred around the growing dendrite arm, as opposed to 2D, where the flow must go over the arm.

6.1. *Solidification of pure materials*

We performed a series of computations where we examined the growth of an isolated dendrite grown from an initial spherical seed. In some cases, a flow (characterized by a far-field velocity U_∞) is directed parallel to the $\langle 100 \rangle$ direction. The results are presented as data for the dendrite tip radius, growth velocity and the selection

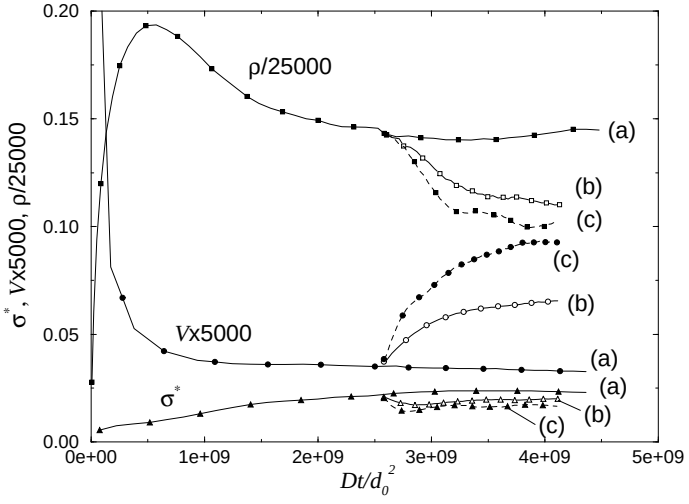

Fig. 22. Evolution of the tip radius (in units of d_o), tip velocity (in units of D/d_o) and selection constant σ^* for the upstream dendrite tip for three cases corresponding to succinonitrile solidification. The data have been multiplied by arbitrary constants for convenience of having them appear on one graph. The cases correspond to (a) no flow; (b) $U_\infty = 0.5$ cm/s; and (c) $U_\infty = 1$ cm/s.

Table 1. Comparison of computed and experimental tip parameters for succinonitrile.

	U_∞ (cm/s)	$V_{\rm tip}/V^0_{\rm tip}$	$\rho_{\rm tip}/\rho^0_{\rm tip}$	σ^*/σ^*_0
Expt	1.0	2.2	0.6	1.4
Calc		2.6	0.72	0.8
Expt	0.5	1.7	0.71	1.2
Calc		2.1	0.71	0.95

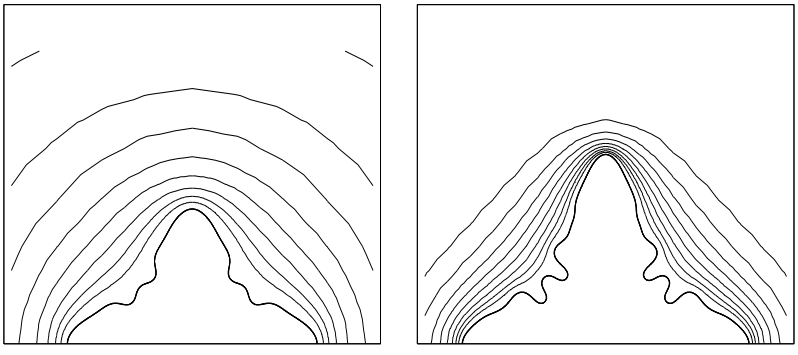

Fig. 23. Interface position and isotherms around the growing dendrite tip for SCN at $Dt/d_o^2 = 4.1 \times 10^9$. Isotherms range from -0.036 to -0.008 in increments of 0.004. The flow from infinity originates from the top of the figure.

constant σ^*. Reported below are calculations corresponding to succinonitrile (SCN), a material with relatively low surface tension anisotropy (0.5%).

The evolution of $\rho_{\rm tip}$, $V_{\rm tip}$ and σ^* for the upstream arm are shown in Fig. 22, multiplied by arbitrary scales for the convenience of plotting them together on one graph. The seed was grown without flow up to $\tilde{D}t/\tilde{d}_o^2 = 2.5 \times 10^9$, and then the flow was started. For this simulation, we have $\tilde{d}_0 = 4.775 \times 10^{-3}$, $\tilde{D} = 116$, $W_o = 1$, $\tau_o = 1$, $\Delta x_{\rm min} = 0.9$, $L_B = 29491.2$ $(= 2^{15}\Delta x_{\rm min})$, $\Delta t = 0.02$, and Pr $= 23.1$.

When the flow begins, $V_{\rm tip}$ increases while $\rho_{\rm tip}$ decreases. The selection constant σ^* decreases, and quickly reaches its steady state value. The simulations were terminated when the mesh size grew to about 450,000 nodes, and while the results have not quite reached a final steady state, the temporal variation is small at the end.

Table 1 compares the computed values of $\rho_{\rm tip}$, $V_{\rm tip}$ and σ^* with experimental data of Lee *et al.*[83] The ratios of tip velocities and tip radii are quite similar in both the simulations and the experiments. However, we find σ^* to be a weakly decreasing function of the far-field velocity, while Lee *et al.*, found σ^* to be an increasing function of U_∞. We attribute this difference to the effect of far field boundary conditions on the results in *both* the experiments and the calculations. See Ref. 80 for details.

The mechanism for the change in tip kinetics due to the flow is illustrated in

Fig. 23. Because the Péclet number is high, the isotherms are advected by the flow, effectively increasing the temperature gradient ahead of the dendrite, and this leads in turn to the increase in tip velocity.

6.2. *Solidification of binary alloys in 3D*

This section describes simulations of solidification in binary alloys in three dimensions. As discussed earlier, one of the most common experimental methods for studying microstructure development in alloys is directional solidification, and we focus on that method here as well. The experiment is normally performed using a transparent alloy confined between microscope slides. A thin section is desired so that the microstructure can be observed easily, and so that the temperature field can be truly 1D. It is observed, however, that under some experimental conditions the microstructure is 3D, while under others it is 2D. We demonstrate via our calculations that the reason for this apparent transition is the interaction of the diffusion field with the boundary imposed by the microscope slides. The results are also compared with experimental data from Liu *et al.*[84]

Simulations of directional solidification were performed in a rectangular domain with dimensions $L_x \times L_y = 256 \times 256$, and variable thickness $\delta \in [4, 64]$. The frozen temperature approximation was applied with a fixed gradient in the x-direction, in a frame moving with fixed velocity $V_p \leq 2$. The units are explained further below.) Simulations started from a nominally flat interface, with random perturbations, and were run until the interface became stationary. A typical computation took about 90 cpu-hours using a single 3.1 GHz Intel processor and compiler.

A directional solidification experiment is characterized by the two dimensionless control parameters, $M = d_o/l_T$ and $S = V_p d_o/D_L$, where d_o is the capillary length, l_T is the thermal length and D_L is the solute diffusivity in the liquid phase; for a pulling velocity of $V_p = 5$ μm/s. To obtain converged results with the phase-field model we require that the solution be independent of the parameter $\epsilon = W_o/d_o$. After ensuring vanishing interface kinetics, the following relationships involving the phase-field parameters are realized: $D\tau_o/W_o^2 = a_1 a_2 \epsilon$, $V_p \tau_o/W_o = S a_1 a_2 \epsilon^2$, and $l_T/W_0 = 1/(\epsilon M)$. Here, $a_1 = 0.8839$ and $a_2 = 0.6267$, are constants that arise in the phase-field formulation, described earlier.[18]

We choose computationally convenient parameters for our study, and then use our understanding of the proper length scales to compare our results with experiments. The parameters used in our study are: $\tau_o = W_o = 1$, $D = 20$, $k = 0.8$, $\epsilon_4 = 0.05$, and $l_T = |m_L|(1-k)C_\infty/kG = 50$; where m_L is the liquidus slope, G is the imposed thermal gradient, and C_∞ is the far field solute concentration. The condition for negligible interface kinetics gives $d_o = 0.0277$ and therefore $\epsilon = 36.1$, which is sufficiently small to ensure convergence.[26] The size of the smallest element in our adaptive mesh is $\Delta x = 1$, when $\delta \geq 8$, and $\Delta x = 0.5$, when $\delta = 4$, while $\Delta t = 0.005$ is the size of the time-step. For these parameter choices, the dimensionless control parameters are $M = 5.54 \times 10^{-4}$ and $S \sim 1.385 \times 10^{-3}$.

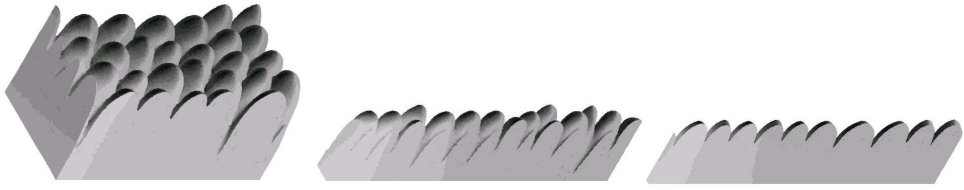

(a) $\delta = 64$, $V_p = 1.5$, 3D cells. (b) $\delta = 16$, $V_p = 1.5$, 3D cells. (c) $\delta = 4$, $V_p = 0.8$, 2D cells.

Fig. 24. Interface morphology in a directionally solidified alloy. At steady state, stable arrays of three-dimensional cells appear. Note that at $\delta = 4$, the array comprises of two-dimensional cells.

Table 2. Physical properties of a SCN-Salol alloy system.

$\|m\|$ (Liquidus slope)	0.7 K/wt.%
D_L (Diffusion coefficient)	8×10^{-10} m^2/s
Γ (Gibbs–Thomson coefficient)	0.64×10^{-7} K/m
k (Partition coefficient)	0.2
G (Thermal gradient)	4 K/mm
d_o (Capillary length)	3.265×10^{-8} m
l_T (Thermal length)	4.9×10^{-4} m

Figure 24 shows examples of computed interface morphologies for different values of δ. For small values of pulling speed ($V_p \leq 2$), the steady state consists of a stationary array shown in Fig. 24. The "peaks" on the interface have sharp and well defined tips, typical of dendrites. There are no sidebranches because the dendrites are quite short, and because there is no noise in the calculations. As pulling velocity increases, the morphology becomes finer, with sharper and more tightly packed cells, consistent with experimental observations.[84–86] Data on tip radius were extracted from representative cells in the structure, and spacing data were obtained using a 3D extension of the FFT technique described earlier for the 2D simulations. For large δ, we find that the tip radii of these cells, measured on the two principal planes, are almost identical. As δ decreases, the radius in the x-z plane becomes significantly smaller, and cross sections of the cells look elliptical. At $\delta = 4$, for small pulling speeds ($V_p \leq 1$), there is a transition to two-dimensional microstructure [Fig. 24(c)].

The data from all of our simulations are shown in Fig. 25, along with experimental data of Liu *et al.*, which corresponds to a SCN-0.7 %wt. Salol system (properties in Table 2). The axes are scaled to enable comparison of the two datasets. The abscissa is the pulling speed (i.e. the tip velocity at steady state) V_{tip}, scaled by a characteristic velocity $D/d_o k$, while the ordinate is the tip radius ρ_{tip}, scaled by the diffusion length D/V_{tip}. The open symbols correspond to the experimental data, and the solid symbols correspond to our calculations, showing very good agreement.

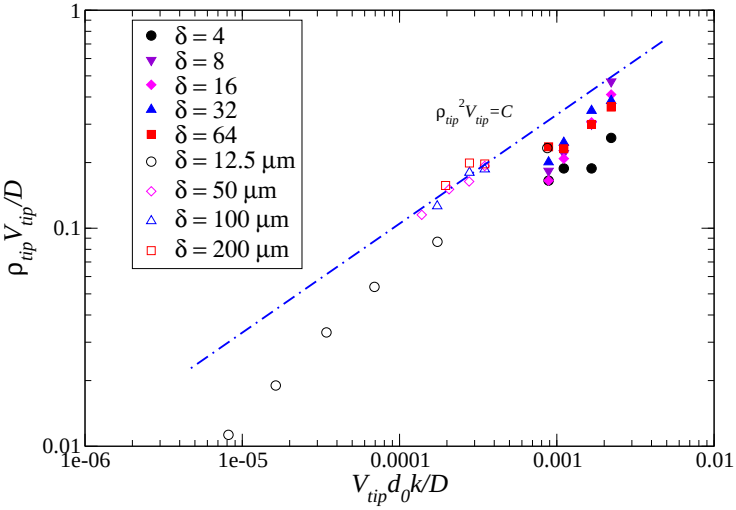

Fig. 25. Comparison of binary alloy simulations with the phase-field model, and experimental data of Liu *et al.*[84] Solid symbols correspond to the phase-field model and the open symbols are experimental data. The line denotes a relationship of the form $\rho_{\rm tip}^2 V_{\rm tip} = C$ between tip radius and velocity, where C can be expressed in terms of process parameters.

Liu *et al.* noted that for 3D microstructures, the tip radius follows a relationship of the form $\rho_{\rm tip}^2 V_{\rm tip} = C$, where C is a constant dependent on d_o, k and D, as postulated by theoretical models of constrained growth.[87,88] However, when δ is of the order of inter-dendritic spacing λ_1, this agreement deteriorates. This is evident in Fig. 25, where the $\rho_{\rm tip}^2 V_{\rm tip} = C$ line is shown as a guide to the eye. The open circles, which are data for $\delta = 12.5$ μm deviate in both slope and intercept from this line, which passes through the rest of their data, indicating a breakdown in the relationship. We observe similar trends in our calculations, where the line $\rho_{\rm tip}^2 V_{\rm tip} = C$ fits our data at $\delta = 32$ and 64 reasonably well, but as δ decreases from 16 to 4, this agreement deteriorates.

Decreasing δ has a pronounced effect on interface morphology. Dendritic arrays seen in experiments have a certain structure/periodicity to them, that arises from underlying crystalline symmetries. For example, in our simulations we observe that the cells constitute a hexagonal array. When δ is large, away from the boundaries the diffusion field surrounding each cell tip obeys this symmetry, and the optimal λ_1 is selected. As δ decreases however, the diffusion field becomes increasingly asymmetric due to interaction with the boundaries at $x = 0$ and $x = \delta$. In particular, solute rejection decreases in the vertical plane x-z, while increasing in the horizontal plane x-y. Increased solute accumulation between cells in x-y, contributes to an increase in λ_1. However, since $V_{\rm tip}$ is fixed by the pulling speed, and a certain rate of solute rejection needs to be maintained, the tips tend to grow sharper as λ_1 increases. It is precisely this effect that causes the operating state to deviate from theoretical predictions.

7. Conclusions

The use of phase field models in materials science has seen a great increase in recent years, owing in part to their fundamental connection to phase-transformations. Nevertheless, phase field models have been difficult to use for quantitative simulations because the inaccuracy brought about by improperly smearing the interface width, to attain practical simulations times and length scales. We have discussed some recent and new work that shows how this problem can be partly overcome through using improved asymptotic analysis of phase field models. These techniques allow one to smear the interface to a large degree but still recover the same kinetics described by sharp interface models of solidification. In addition, we reviewed recent numerical algorithms that use dynamic adaptive mesh refinement to enable a dramatic increase in simulation system sizes, as well as a great decrease in computation times.

We reviewed dendritic growth in 2D and 3D simulations made using phase field models simulated with the DAMR method. 2D simulations have investigated the role of inter-dendritic interactions at low undercooling, finding that dendritic growth and morphology is described through a dynamic crossover scaling formalism. Likewise DAMR simulations of directionally solidified binary alloys predicted that primary dendrite branch spacing is described through a single universal scaling function over a range of alloy concentrations and cooling rates and thermal gradient. We also reviewed recent results that elucidate how the interaction of thermal gradient and surface tension anisotropy lead to seaweed crystal structure. 3D simulations elucidated the role of fluid flow on the stability parameter σ^* of microscopic solvability theory. Simulations of directionally solidified alloys in 3D found that as 3D cells were confined to smaller spaces in the z-direction, there was a transition from a 3D to a 2D behavior.

References

1. D. Askeland, *The Science of Materials and Engineering* (Thomson, Brooks/Cole, Belmont, CA, 2003).
2. W. Kurz and D. J. Fisher, *Fundamentals of Solidification* (Trans Tech, Aedermannsdorf, Switzerland, 1992).
3. J. S. Langer, *Rev. Mod. Phys.* **52**, 1 (1980).
4. N. A. Ahmad, A. A. Wheeler, W. J. Boettinger and G. A. McFadden, *Phys. Rev. E* **58**, 3436 (1989).
5. J. C. Baker and J. D. Cahn, *Solidification* (ASM, Metals Park, OH, 1971), p. 23.
6. M. Hillert and B. Sundman, *Acta Metall.* **24**, 731 (1976).
7. M. J. Aziz and T. Kaplan, *Acta Metall.* **36**, 2335 (1988).
8. M. J. Aziz and W. J. Boettinger, *Acta Metall. Mater.* **42**, 257 (1994).
9. W. J. Boettinger and M. J. Aziz, *Acta Metall.* **37**, 3379 (1989).
10. Z. K. Liu, in *Solid-Solid Transformations*, eds. W. C. Johnson, J. M. Howe, D. E. Laughlin and W. A. Soffa (The Minerals, Metals and Materials Society, Warrendale, PA, 1994), p. 219.
11. M. Haataja, J. Mahon, N. Provatas and F. Leonard, *J. Appl. Phys.* (2005) (in press).

12. J. B. Collins and H. Levine, *Phys. Rev. B* **31**, 6119 (1985).
13. P. Kopczynski, W. J. Rappel and A. Karma, *Phys. Rev. E* **55**, 1282 (1997).
14. N. Provatas and J. Dantzig, *The Enyclopedia of Materials Science and Technology* (Elsevier Science Ltd., Oxford, 2001).
15. N. Provatas, Q. Wang, M. Haataja and M. Grant, *Phys. Rev. Lett.* **91** 155502 (2003).
16. R. Trivedi, S. Liu, B. Echebarria and A. Karma, *TMS* (2004).
17. K. R. Elder, M. Grant, N. Provatas and M. Kosterlitz, *Phys. Rev. E* **64**, 1604 (2001).
18. A. Karma and W.-J. Rappel, *Phys. Rev. E* **53**, 3017 (1996).
19. Y.-T. Kim, N. Provatas, J. Dantzig and N. Goldenfeld, *Phys. Rev.* **59**, 2546 (1999).
20. G. Caginalp and W. Xie, *Phys. Rev. E* **48**, 1897 (1993).
21. P. C. Hohenberg and B. I. Halperin, *Rev. Mod. Phys.* **49**, 435 (1977).
22. Y. Kim, N. Provatas, N. Goldenfeld and J. Dantzig, *Phys. Rev. E* **59**, 2546 (1999).
23. J. A. Warren and W. J. Boettinger, *Acta Metall. Mater. A* **43**, 689 (1995).
24. J.-H. Jeong, N. Goldenfeld and J. A. Dantzig, *Phys. Rev. E* **64**, 041602 (2001).
25. W. J. Boettinger, J. A. Warren, C. Beckermann and A. Karma, *Ann. Rev. Mater. Res.* **32**, 163 (2002).
26. B. Echebarria, R. Folch, A. Karma and M. Plapp, *Phys. Rev. E* **70**, 061604 (2004).
27. G. Caginalp, *Arch. Rat. Mech. Anal.* **92**, 205 (1986).
28. R. Almgren, *SIAM J. Appl. Math.* **59**, 2086 (1999).
29. Chakin and Lubensky, *Principles of Condensed Matter Physics* (North Holland, Amsterdam, 1987), p. 629.
30. N. Provatas, J. Dantzig, and N. Goldenfeld, *Phys. Rev. Lett.* **80**, 3308 (1998).
31. N. Provatas, J. Dantzig and N. Goldenfeld, *J. Comp. Phys.* **148**, 265 (1999).
32. M. Plapp and A. Karma, *J. Comp. Phys.* **165**, 592 (2000).
33. M. Plapp and A. Karma, *Phys. Rev. Lett.* **84**, 1740 (2000).
34. K. R. Elder, F. Drolet, J. M. Kosterlitz and M. Grant, *Phys. Rev. Lett.* **72**, 677 (1994).
35. M. Plapp and A. Karma, *Phys. Rev. E* **66**, 061608 (2002).
36. A. Karma, *Phys. Rev. Lett.* **87**, 115701 (2001).
37. M. Greenwood, M. Haataja and N. Provatas, *Phys. Rev. Lett.* **93**, 246101 (2004).
38. J. C. Ramirez and C. Beckermann, *Acta Mater.* **53**, 1721 (2005) .
39. J. W. Cahn and J. E. Hilliard, *J. Chem. Phys.* **28**, 258 (1958).
40. J. W. Cahn and J. E. Hilliard, *J. Chem. Phys.* **31**, 688 (1959).
41. R. Tönhardt and G. Amberg, *J. Crystal Growth* **194**, 406 (1998).
42. D. Juric, in *Modeling of Casting, Welding and Advanced Soldification Processes*, eds. B. G. Thomas and C. Beckermann (TMS-AIME, San Dieago, USA, 1998), pp. 605–612.
43. C. Beckermann, H.-J. Diepers, I. Steinbach, A. Karma and X. Tong, *J. Comp. Phys.* **154**, 468 (1999).
44. P. M. Gresho, S. T. Chan, M. A. Christon and A. C. Hindmarsh, *Int. J. Numer. Methods Fluids* **21**, 837 (1995).
45. N. Provatas, T. Ala-Nissila, M. Grant, K. P. Elder and L. Pichẽ, *J. Stat. Phys.* **81**, 737 (1995).
46. H. J. Neeman, (University of Illinois, 1996).
47. A. Schmidt, *J. Comp. Phys.* **125**, 293 (1996).
48. P. R. B. Devloo, Ph.D Thesis, University of Texas at Austin, Austin, TX, 1987.
49. M. S. Shephard, P. L. Baehmann and K. R. Grice, *Comm. App. Num. Meth.* **4**, 379 (1988).
50. N. Palle and J. A. Dantzig, *Met. Trans. A* **27**, 707 (1996).
51. R. D. Cook, D. D. Malkus, M. E. Plesha and R. J. Witt, *Concepts and Applications of Finite Element Analysis* (John Wiley, New York, USA, 2002).

52. O. C. Zienkiewicz and J. Z. Zhu, *Int. J. Numer. Meth. Eng.* **24**, 337 (1987).
53. L. V. Kale and S. Krishnan, *Parallel Programming using C++*, eds. G. V. Wilson and P. Lu (MIT Press, USA, 1996), p. 175.
54. M. Bhandarkar and L. V. Kalé, *Proc. Int. Conf. on High Performance Computing* (*HiPC*), Vol. 1970, eds. M. Valero, V. K. Prasanna and S. Vajpeyam (Springer-Verlag, Berlin, Heidelberg, December 2000).
55. G. P. Ivantsov, *Dokl. Akad. Nauk USSR* **58**, 1113 (1947).
56. D. A. Kessler and H. Levine, *Phys. Rev. E* **31**, 1712 (1985).
57. E. Ben-Jacob, N. Goldenfeld, B. G. Kotliar and J. S. Langer, *Phys. Rev. Lett.* **53**, 2110 (1984).
58. J. S. Langer, *Directions in Condensed Matter* (World Scientific, Singapore, 1986), p. 164.
59. D. Kessler, J. Koplik and H. Levine, *Phys. Rev. A* **30**, 3161 (1984).
60. M. Sabouri-Ghomi, N. Provatas and M. Grant, *Phys. Rev. Lett.* **86**, 5084 (2001).
61. Y. Lu, C. Beckermann and A. Karma, *Proc. IMECE2002*, (2002).
62. X. Tong, C. Beckermann, A. Karma and Q. Li, *Phys. Rev. E* **63**, 1063 (2001).
63. H. Lowen, J. Bechhoefer and L. S. Tuckerman, *Phys. Rev. A* **45**, 2399 (1992).
64. M. Conti, *Phys. Rev. E* **55**, 765 (1997).
65. Y. B. Altundas and G. Caginalp, *J. Stat. Phys.* **110**, 1055 (2003).
66. N. Provatas, J. Dantzig, N. Goldenfeld, J. C. Lacombe, A. Lupulescu, M. B. Koss and M. E. Glicksman, *Phys. Rev. Lett.* **82**, 4496 (1999).
67. R. Almgren, W. S. Dai and V. Hakim, *Phys. Rev. Lett.* **71**, 3461 (1993).
68. R. Trivedi and K. Somboonsuk, *Mat. Sci. Eng.* **65**, 65 (1983).
69. J. Bechhoefer and A. Libchaber, *Phys. Rev. B* **35**, 1393 (1987).
70. R. Trivedi and W. Kurz, *Acta Metall. Mater.* **42**, 15 (1994).
71. J. S. Kirkaldy, L. X. Liu and A. Kroupa, *Acta Metall. Mater.* **43**, 2905 (1995).
72. L. X. Liu and J. S. Kirkaldy, *Acta Metall. Mater.* **43**, 2891 (1995).
73. W. Losert, B. Q. Shi and H. Z. Cummins, *Proc. Natl. Acad. Sci. (USA)* **95**, 431 (1998).
74. W. Losert, O. N. Mesquita, J. M. A. Figueiredo and H. Z. Cummins, *Phys. Rev. Lett.* **81**, 409 (1998).
75. B. Utter, R. Ragnarsson and E. Bodenschatz, *Phys. Rev. Lett.* **86**, 4604 (2001).
76. D. Jasnow and J. Vinals, *Phys. Rev. A* **41**, 6910 (1990).
77. W. Kurz and D. J. Fisher, *Acta Metall.* **29**, 11 (1981).
78. S. Akamatsu, G. Faivre and T. Ihle, *Phys. Rev. E* **51**, 4751 (1995).
79. T. Ihle and H. Muller-Krumbhaar, *Phys. Rev. Lett.* **70**, 3083 (1993).
80. J.-H. Jeong, J. A. Dantzig and N. Goldenfeld, *Met. Mater. Trans.* **34A**(3), 459 (2003).
81. B. P. Athreya and J. A. Dantzig, Dendritic Growth in Confined Spaces, *Phil. Mag.* (2005), to appear.
82. J. A. Dantzig and L. S. Chao, *Solidification Processing*, ed. H. Jones (1987), p. 502.
83. Y.-W. Lee, R. Ananth and W. N. Gill, *J. Cryst. Growth* **132**, 226 (1993).
84. S. Liu, R. Trivedi, B. P. Athreya and J. A. Dantzig, unpublished.
85. K. Somboonsuk, J. T. Mason and R. Trivedi, *Met. Trans. A* **15**, 967 (1984).
86. L. X. Liu and J. S. Kirkaldy, *J. Cryst. Growth* **140**, 115 (1994).
87. R. Trivedi, *J. Cryst. Growth* **49**, 219 (1980).
88. W. Kurz and D. J. Fisher, *Fundamentals of Solidification* (Trans Tech Publications, Switzerland, 1989), 3rd edn.